

Time-resolved cryo-EM of G-protein activation by a GPCR

<https://doi.org/10.1038/s41586-024-07153-1>

Received: 27 March 2023

Accepted: 2 February 2024

Published online: 13 March 2024

 Check for updates

Makaia M. Papasergi-Scott¹, Guillermo Pérez-Hernández², Hossein Batebi³, Yang Gao¹, Gözde Eskici¹, Alpay B. Seven¹, Ouliana Panova¹, Daniel Hilger^{1,4}, Marina Casiraghi^{1,5}, Feng He¹, Luis Mau⁶, Peter Gmeiner⁶, Brian K. Kobilka¹, Peter W. Hildebrand^{2,3,7} & Georgios Skiniotis^{1,8}✉

G-protein-coupled receptors (GPCRs) activate heterotrimeric G proteins by stimulating guanine nucleotide exchange in the $\text{G}\alpha$ subunit¹. To visualize this mechanism, we developed a time-resolved cryo-EM approach that examines the progression of ensembles of pre-steady-state intermediates of a GPCR–G-protein complex. By monitoring the transitions of the stimulatory G_s protein in complex with the β_2 -adrenergic receptor at short sequential time points after GTP addition, we identified the conformational trajectory underlying G-protein activation and functional dissociation from the receptor. Twenty structures generated from sequential overlapping particle subsets along this trajectory, compared to control structures, provide a high-resolution description of the order of main events driving G-protein activation in response to GTP binding. Structural changes propagate from the nucleotide-binding pocket and extend through the GTPase domain, enacting alterations to $\text{G}\alpha$ switch regions and the $\alpha 5$ helix that weaken the G-protein–receptor interface. Molecular dynamics simulations with late structures in the cryo-EM trajectory support that enhanced ordering of GTP on closure of the α -helical domain against the nucleotide-bound Ras-homology domain correlates with $\alpha 5$ helix destabilization and eventual dissociation of the G protein from the GPCR. These findings also highlight the potential of time-resolved cryo-EM as a tool for mechanistic dissection of GPCR signalling events.

G-protein-coupled receptors (GPCRs) relay extracellular signals primarily via the activation of distinct subtypes of heterotrimeric G proteins (consisting of $\text{G}\alpha$, $\text{G}\beta$ and $\text{G}\gamma$ subunits), which in turn initiate signalling cascades by interacting with downstream effectors. For the vast majority of GPCRs, agonist binding to the receptor extracellular pocket promotes conformational changes on the intracellular side, enabling the engagement of the GDP-bound $\text{G}\alpha$ subunit of a G-protein heterotrimer (Fig. 1a). A key player in this receptor–G-protein interaction is the $\text{G}\alpha$ C-terminal $\alpha 5$ helix, which must undergo a conformational transition to engage the receptor². The repositioning of the $\alpha 5$ helix, in conjunction with the disengagement of the α -helical domain (AHD) from the Ras-homology domain (RHD)^{3,4}, leads to a weaker affinity for, and release of, GDP^{4,5}. The nucleotide-free G protein is subsequently loaded with GTP, promoting structural changes that activate $\text{G}\alpha$, weaken its affinity for the receptor and drive the functional dissociation of the G-protein heterotrimer^{6–9}.

Although the pathway from receptor agonism to G-protein activation is a dynamic, multistep mechanistic process^{4,10–14}, structural studies have been very limited in capturing different substates. Since the initial crystal structure of β_2 -adrenergic receptor ($\beta_2\text{AR}$) in complex with G_s protein², the advent of cryo-electron microscopy (cryo-EM) has

facilitated many structures of GPCR–G-protein complexes^{15–17}, providing a wealth of information on ligand recognition, receptor activation and G-protein coupling. The G protein has the highest affinity for the receptor in the absence of nucleotide, and therefore nucleotide-free conditions have invariably been used for structural studies to promote receptor complex stability, which is often further enhanced with stabilizing nanobodies or antibodies^{16,18}. However, given the constant presence of nucleotides in the cytoplasm, a nucleotide-free GPCR–G protein is probably extremely transient in vivo, and thus these structures provide a very narrow window into the G-protein activation process. Yet to be captured are short-lived transition intermediates associated with G-protein coupling, GDP release and GTP binding, leading to activation of the G-protein heterotrimer and its functional dissociation from a GPCR. Such structural information is critical to outline the conformational landscape of the dynamic GPCR signalling systems, to understand the basis for G-protein selectivity¹⁹ and to evaluate the effects of drugs with distinct efficacies and potencies to enable more rational pharmacology²⁰.

To address this limitation, we sought to visualize by cryo-EM the transition of conformational ensembles of $\beta_2\text{AR}$ in complex with heterotrimeric G_s protein after adding GTP. The $\beta_2\text{AR}$ belongs to the largest family

¹Department of Molecular and Cellular Physiology, Stanford University School of Medicine, Stanford, CA, USA. ²Charité-Universitätsmedizin Berlin, Corporate Member of Freie Universität Berlin and Humboldt-Universität zu Berlin, Institute of Medical Physics and Biophysics, Berlin, Germany. ³Institute of Medical Physics and Biophysics, Faculty of Medicine, Leipzig University, Leipzig, Germany. ⁴Institute of Pharmaceutical Chemistry, Philipps-University of Marburg, Marburg, Germany. ⁵Dipartimento di Bioscienze, Università degli Studi di Milano, Milan, Italy. ⁶Department of Chemistry and Pharmacy, Medicinal Chemistry, Friedrich-Alexander University Erlangen-Nürnberg, Erlangen, Germany. ⁷Berlin Institute of Health at Charité-Universitätsmedizin Berlin, Berlin, Germany. ⁸Department of Structural Biology, Stanford University School of Medicine, Stanford, CA, USA. ✉e-mail: yiorgos@stanford.edu

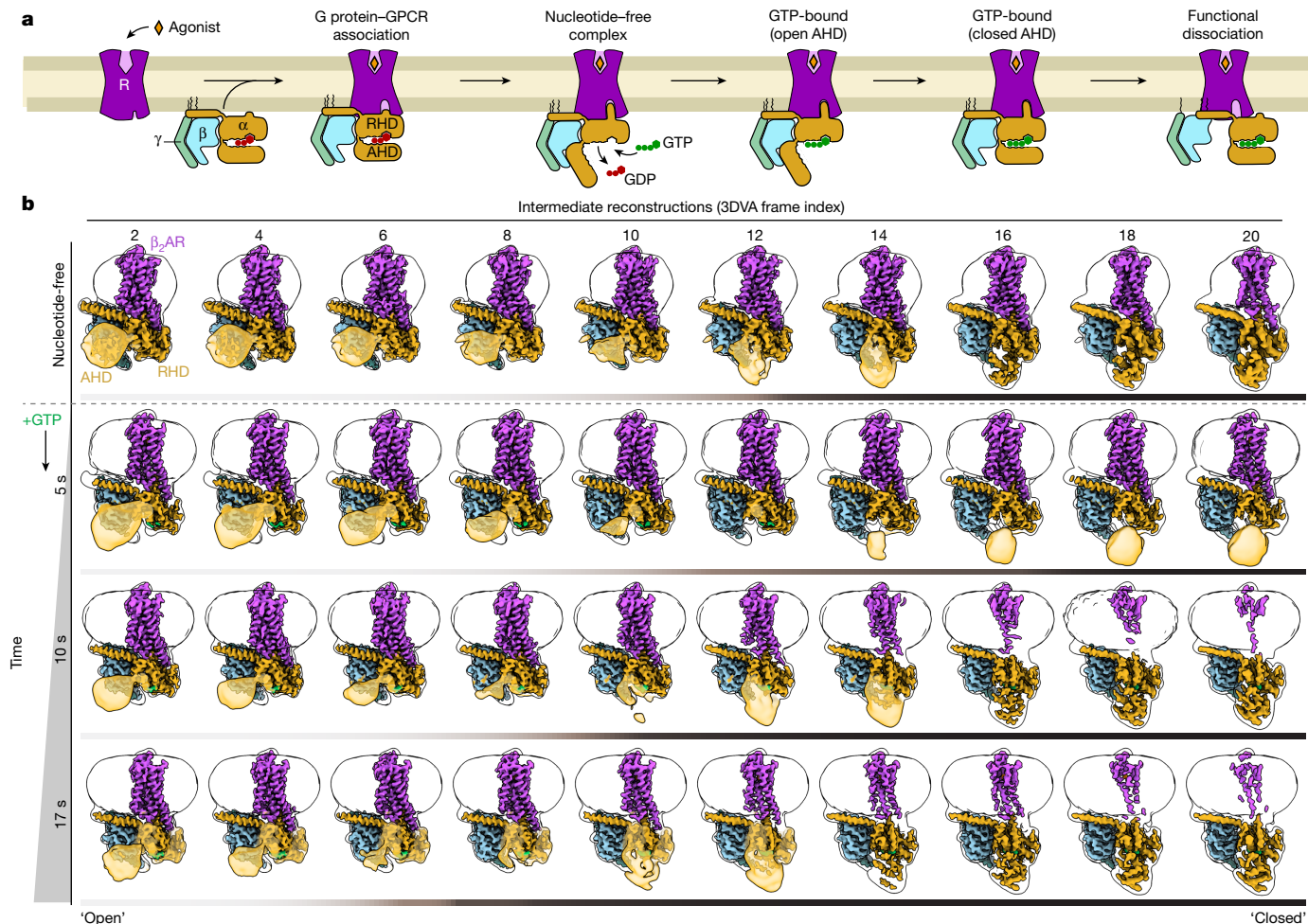


Fig. 1 | Conformational dynamics during G-protein activation. **a**, In response to agonist binding, a GPCR engages heterotrimeric G protein through the G α C-terminal α 5 helix, resulting in the displacement of the G α AHD in relation to the RHD. This opening allows for the release of bound GDP and the subsequent binding of GTP, leading to G α subunit activation and functional dissociation of G β γ from G α . **b**, $\beta_2\text{AR}-G_s$ conformational dynamics revealed through cryo-EM. Complexes were captured by vitrification in the nucleotide-free state. Using the 3DVA function of cryoSPARC, the data were divided to obtain 20 reconstructions across the major principal component of motion (that is, AHD closure). For space consideration, only even-numbered intermediates (frame indexes) are shown.

Complexes were additionally frozen at progressive time points following the addition of GTP to the nucleotide-free complex (last three rows). Using the same processing schema, the dynamics of the GTP-bound complex revealed the proportion of particles with a closed AHD to increase with time of vitrification post addition of GTP. Reconstructions shown include the sharpened maps in solid colour, surrounded by the Gaussian-filtered unsharpened envelope to show the micelle and location of the AHD (translucent gold, except when observed directly in the sharpened map). Colour bars beneath each structural ensemble are shaded in relation to the observation of the 'open' or 'closed' AHD position.

of GPCRs, family A, and primarily couples to G $_s$ to increase intracellular cAMP levels²¹, thereby regulating crucial physiological responses, such as smooth muscle relaxation and bronchodilation^{22–24}. The $\beta_2\text{AR}-G_s$ signalling system has been historically well studied, providing various lines of biochemical, biophysical and structural data that can support mechanistic investigations^{2,6,10–12,25–27}. Our early EM analysis of $\beta_2\text{AR}-G_s$ using negative-stain 'fixation trapping', on EM grids within several seconds after adding GTPyS⁶, revealed distinct complex dissociation intermediates. Although at low resolution, that work provided a valuable demonstration that such direct visualization is feasible without pursuing sample mixing and freezing at the millisecond timescale. Inspired by these studies, here we used cryo-EM and 'freeze trapping' at distinct time points after the addition of GTP to examine ensembles of $\beta_2\text{AR}-G_s$ complex and reconstruct several ordered states from conformationally heterogeneous complexes. By monitoring how distinct structural populations evolved over time compared with 'checkpoint' crystal structures, we were able to capture, with high resolution, the ordering of key events underlying G-protein activation on the receptor. This time-resolved cryo-EM approach to visualize pre-steady-state

$\beta_2\text{AR}-G_s$ -GTP intermediates presents both opportunities and challenges for exploring key molecular recognition events underlying the highly tuned GPCR signalling mechanisms.

Conformational dynamics of the nucleotide-free complex

In a first study, we evaluated the dynamic behaviour of detergent-solubilized nucleotide-free $\beta_2\text{AR}-G_s$ complex ($\beta_2\text{AR}-G_s^{\text{EMPTY}}$) by cryo-EM, further aiming to establish a baseline for complex stability under these conditions. To capture the full dynamic range of complex conformations, we chose not to use any single-chain variable fragment (scFv) or nanobody stabilizers. Instead, we enhanced sample stability by activating the receptor with c-Epi, a conformationally constrained epinephrine that is a highly efficacious and $\beta_2\text{AR}$ -selective agonist²⁸. Previous studies, including our earlier EM work with negative-stained particles, revealed the dynamic positioning of AHD in the $\beta_2\text{AR}-G_s^{\text{EMPTY}}$ complex^{4,6}. Similarly, in our current cryo-EM study, a conventional three-dimensional (3D) particle classification approach shows different

locations of the AHD as it flexes between open and closed conformations around the RHD (Extended Data Fig. 1a). To better explore these conformations and their transitions, we used 3D variability analysis (3DVA)²⁹ as implemented in cryoSPARC, which clusters and orders projections on the basis of particle conformation along principal components of variability, thereby enabling a view of the main directions of macromolecular dynamics observed in a complex (Fig. 1, Extended Data Fig. 1, Supplementary Tables 1 and 2, Supplementary Fig. 1 and Supplementary Videos 1 and 2). The first principal component (PCO), split into 20 frames that include weighted overlapping particles from adjacent frames, shows an extensive swing-like movement of the density corresponding to the AHD between a fully open and a fully closed position against the RHD. By using the subsets of particles contributing to each frame we generated 20 ‘transitional’ cryo-EM reconstructions with global indicated resolutions between 3.2 Å and 4.2 Å (Fig. 1, Extended Data Fig. 1, Supplementary Tables 1 and 2, Supplementary Figs. 1 and 2 and Supplementary Videos 1 and 2). As these subsets appeared to represent a continuous variability in positioning and no ordering of the AHD in different locations, we chose to use a windowing value of 2 for particle projection overlap between adjacent frames, thereby also improving the resolution by increasing the number of projections used to reconstruct each map. A windowing value of 0 (discrete sorting), 1 or 2 in 3DVA produced similar reconstructions, as judged by the overall model fit, albeit with an impact on resolution for smaller windowing of frames (Supplementary Table 3 and Supplementary Fig. 3). Of note, there are predominantly two overall locations of the AHD, open versus closed, with limited occupancy of transitions between them (Fig. 1b and Extended Data Figs. 1 and 2). By contrast, the rest of the complex along this primary principal component appears overall conformationally stable (Supplementary Fig. 1 and Supplementary Table 2).

In the most open conformations, the cryo-EM density of the AHD pivots away from its closed position by approximately 61° and lies adjacent to the 2nd and 3rd propeller blades of the G β subunit (Extended Data Fig. 2). This is different from its position in the β_2 AR–G $_s$ crystal structure (Extended Data Fig. 2h), in which the AHD is further pivoted away from the RHD (approximately 88°) to enable its interaction with the 1st and 2nd blades of the β -propeller, a difference that could arise, at least in part, from crystal packing. The cryo-EM structure of NTSR1–G $_i$ (PDB 7LOQ)³⁰ also resolves the open G i AHD adjacent to the 2nd and 3rd G β blades, although seemingly in a distinct orientation from that of the β_2 AR–G $_s$ cryo-EM structure, a deviation that probably stems from differences in the G α subtype. The analysis of the conformational variability of the β_2 AR–G $_s$ complex in its nucleotide-free form provided a baseline to compare the conformational dynamics of the complex under all other conditions probed in this study. Nevertheless, in a cellular context, the nucleotide-free state is unlikely to exist for any significant length of time, as the high concentration of GTP (approximately 300 μ M, compared to about 36 μ M GDP³¹) in human cells drives immediate nucleotide binding with subsequent G-protein activation and functional dissociation from the receptor⁶.

Sequential freeze trapping for time-resolved cryo-EM of β_2 AR–G $_s$ –GTP

G-protein activation in response to GPCR activation in cells occurs in less than a second^{32,33}, but the process is slowed substantially to several seconds when the receptor is solubilized in detergent³⁴. Although this highlights the importance of a native cellular environment, the *in vitro* reconstituted complexes afford us the opportunity to explore the mechanics of activation in a slowed system. To visualize the molecular changes leading to G-protein activation and functional release from the receptor following nucleotide binding, we developed a time-resolved cryo-EM approach whereby we vitrified and imaged detergent-solubilized β_2 AR–G $_s$ complex at short sequential time points (5 s, 10 s and 17 s) post addition of GTP at 4 °C. The 3DVA analysis, as

implemented above, revealed a range of complex conformations analogous to the nucleotide-free complex but with two notable differences. First, the population of particles with a closed AHD conformation increases progressively with the time of GTP incubation before freeze trapping. Second, the later frames in the trajectories for 10 s and 17 s show disappearing receptor densities, suggesting complex destabilization (Fig. 1b, Extended Data Figs. 2–5, Supplementary Fig. 1, Supplementary Tables 2 and 4 and Supplementary Videos 3–5), as also supported by direct negative-stain EM visualization of complex dissociation in most of our sample by 20 s (Supplementary Fig. 4).

To verify that the 3DVA resulted from properly ordered structural transitions, and to classify the conformers from different time points within the same PCA trajectory, we merged the curated β_2 AR–G $_s$ ^{GTP} particles of all time points together and processed this larger dataset by 3DVA to obtain 20 ordered reconstructions from overlapping particle distributions with global indicated resolutions of 2.9 Å–3.6 Å (Fig. 2, Extended Data Fig. 6, Supplementary Table 1, Supplementary Fig. 5 and Supplementary Videos 6 and 7). Like the β_2 AR–G $_s$ ^{EMPTY} and individual β_2 AR–G $_s$ ^{GTP} datasets, we observed that the position of the AHD remained the most recognizable primary variable across the trajectory, proceeding from an open AHD conformer to a closed AHD conformer (Extended Data Fig. 2). Moreover, when each intermediate reconstruction frame was analysed to determine the time stamp of particles, it became apparent that projections from our shortest time point (5 s) contributed more to the frames with an open AHD (early intermediate reconstructions), with minimal contributions to late frames in the trajectory (Fig. 2 and Extended Data Fig. 6). By contrast, as the conformers progressed to a closed AHD position (ordering from intermediate 1 to 20) we observed increasing contribution from the later time-point datasets (that is, 10 s followed by 17 s) (Fig. 2b). The expected distribution of particles from individual datasets with increasing time across the combined trajectory supports the relative robustness of our approach despite the limited features of the rather small membrane protein complex. Furthermore, the merging of datasets enabled us to increase the number of projections contributing to every conformation, potentially improving the projection classification and the resolution of each intermediate map. These results, combined with comparisons to known structures detailed below, further enhanced our confidence that the conformational transitions underlying the 3DVA trajectory stem from temporal, coordinated dynamics rather than stochastic motions following the addition of GTP. In further support, the combined GTP dataset was also processed using conventional 3D classification, which showed the same trend in temporal conformational transitions and the correlation between AHD closure and destabilization of the receptor–G-protein interface (Extended Data Fig. 7, Supplementary Figs. 1, 6 and 7, Supplementary Tables 1, 2 and 5 and Supplementary Video 8). A mask encompassing the G-protein dynamic range was used for 3D classification without alignment into 20 discrete classes (classes A–T). Ordering of these classes by increasing contribution from the 17 second dataset reveals a general trend in reconstructions from an open AHD state to a closed AHD state, as was the case with the 3DVA (Extended Data Figs. 2 and 7, Supplementary Figs. 6 and 7, Supplementary Video 8 and Supplementary Table 5).

Consistent with diffusion-limited binding of nucleotide to the G protein, density for GTP is clearly observed within the nucleotide-binding pocket across all frames in the 3DVA trajectory, but the AHD becomes stabilized into a closed conformation only in later frames (Fig. 2, Extended Data Figs. 2 and 6, Supplementary Fig. 5 and Supplementary Video 7). From a cursory vantage point, the β_2 AR–G $_s$ ^{EMPTY} and β_2 AR–G $_s$ ^{GTP} trajectories appear similar in the AHD motion from an ‘open’ to a ‘closed’ position (Fig. 1b and Extended Data Fig. 8). However, the positioning of the ‘closed’ AHD in relation to the RHD deviates by 17° (as measured by change in the α A helix) between the nucleotide-free and GTP conditions (Extended Data Fig. 8). The variable positioning of the AHD regardless of the presence of nucleotide suggests a passive role

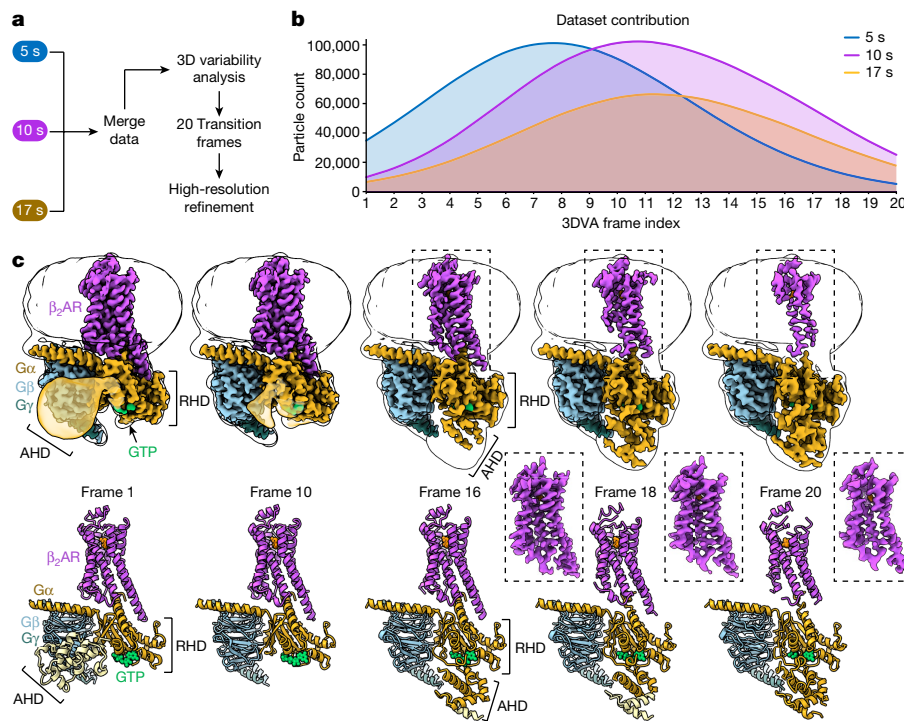


Fig. 2 | Changes in G α structure initiated by GTP binding. **a**, Individual, curated β_2 AR–G α ^{GTP} datasets were combined and processed together to produce a consensus 3DVA trajectory. **b**, A query of the contribution of individual datasets to each intermediate reconstruction (frame) revealed that early intermediates (open AHD) consist primarily of particles from the earliest time point (5 s), and later time points (10 and 17 s) correspond increasingly to later intermediate reconstructions (closed AHD). **c**, Selected cryo-EM reconstructions (top) and models (bottom) resulting from merging β_2 AR–G α ^{GTP} datasets. Note that: (1) density for GTP (green) is clearly present across the entire trajectory; and

(2) as the AHD domain transitions to a closed conformation and becomes more stabilized (that is, density appears), the density for the transmembrane helices of β_2 AR appears progressively weaker at the same contour level, suggesting flexibility of the receptor as it relates to the G-protein heterotrimer. Local refinement of the receptor density alone produces maps with stable features throughout the 7TM, shown in dashed boxes. The AHD in the frame 1 ribbon structure (bottom left panel) is coloured pale yellow as the domain could be rigidly docked into the EM map shown in the top left panel, but it is absent in the deposited molecular model.

for GTP in AHD closure. As the AHD samples both the open and closed states relatively equally in the nucleotide-free state (Extended Data Fig. 2), we infer that the binding of GTP does not allosterically trigger AHD closure; rather, the presence of GTP locks the AHD against the RHD domain as the AHD stochastically samples the closed conformation. Reciprocally, the fully closed AHD promotes further stabilization of GTP within the nucleotide-binding site, with the nucleotide participating in salt bridge interactions between the AHD and RHD. The AHD must be open for the initial binding of nucleotide to the RHD^{4,6}, and our maps collectively suggest that GTP can remain engaged to its binding site without the immediate closure of the AHD, consistent with studies using non-functional constructs of G α lacking the AHD^{35–37} or other small GTPases lacking a helical domain (for example, Ras, Rab, Rho)³⁸. This also points to a connection between AHD dynamics and the kinetics of G-protein activation, a correlation that is suggested by the activity differences observed between the G α long versus short isoforms³⁹, which only differ in the length of a linker connecting the Ras to the AHD. Notably, the ability of the plant homologue GPA1 to self-activate has also been attributed to a greater range of motion and frequency of closure of the AHD relative to the RHD⁴⁰. Significant changes in the RHD and its interaction with the receptor occur only after the AHD has closed. One of the striking observations of our analysis is that the ordering and full closure of the AHD correlates with a decrease in resolvable density of the β_2 AR transmembrane region (Fig. 2 and Extended Data Fig. 6). Notably, this phenomenon is not observed in the structures of the nucleotide-free complex, suggesting a significant change in interactions between receptor and G protein in response to G-protein activation by GTP.

Sequential G-protein rearrangements in response to GTP loading

The cryo-EM maps from overlapping particle subsets across the variability trajectory of the combined dataset enabled us to generate 20 average structures representing GTP-driven transitions coincident with the closure of the G α AHD (Fig. 2c, Supplementary Fig. 5, Supplementary Table 5 and Supplementary Video 9 and 10). To further investigate how the binding of GTP at the nucleotide site triggers G-protein activation and disengagement from the receptor, we analysed the main dynamic events occurring across these structures. Starting from the GTP-binding site, we observe that in initial frames with a fully open AHD, the phosphate tail of GTP maintains weak interactions with residues of the α 1 helix and the highly conserved P loop⁴¹ (β 1– α 1) of the G α s RHD, whereas the GTP purine ring is stabilized through backbone contacts with the TCAT loop (β 6– α 5) and the hinge between the β 5 strand and α G helix (Fig. 3 and Supplementary Fig. 8). The TCAT loop connects the β 6 strand to the α 5 helix, which is the primary G-protein element engaging the receptor. As the transition progresses, the GTP phosphate tail becomes further stabilized by the P loop with an associated translation of the nucleotide by approximately 2 Å within the binding pocket (Fig. 3 and Supplementary Fig. 8) and a corresponding change of the conformation of the TCAT loop that follows the movements of the purine ring (Fig. 3). The stabilization of GTP–P loop interactions correlates with an extension by 1.5 helical turns of the α 1 helix, which directly connects to the AHD (Supplementary Table 4). This extension of the α 1 helix seems to require the presence of nucleotide, as it is not observed in the β_2 AR–G α ^{EMPTY} trajectory. Notably, in the nucleotide-free

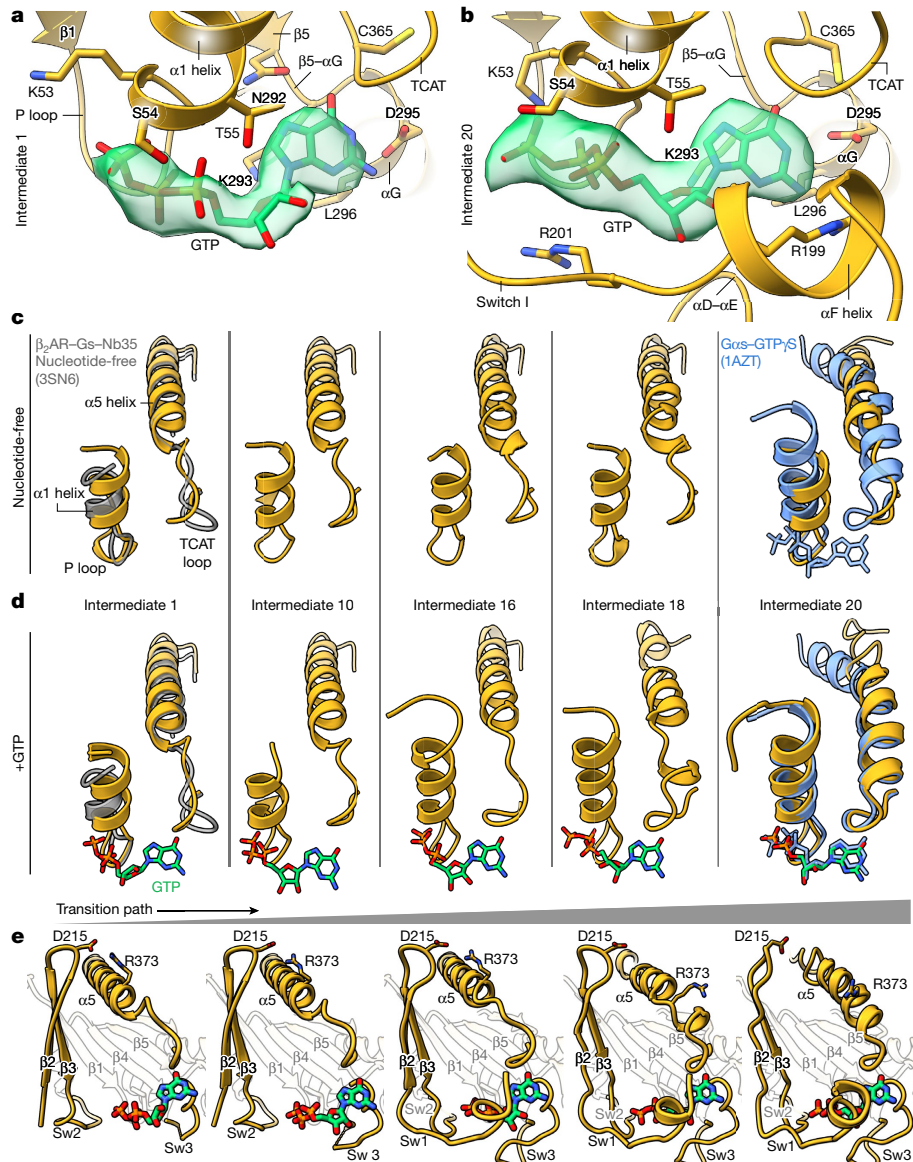


Fig. 3 | Cryo-EM structures reveal transition intermediates between steady-state structures of nucleotide-free G α s and activated G α s-GTPyS. **a, b**, Comparison of the GTP-binding site between the first (**a**) and last (**b**) intermediates resolved by 3DVA analysis. Cryo-EM density for modelled GTP is shown in translucent green. **c**, Closure of the AHD alone does not promote notable changes to the RHD elements (α 1 and α 5). **d**, By contrast, the presence

of nucleotide induces movement of the TCAT motif and extension of the α 1 helix. **e**, Over the transition path to activation, the switch regions (SwI–SwIII) become stabilized towards the nucleotide-binding site. An ionic lock between the β 2– β 3 loop and α 5 helix breaks as the α 5 helix shifts to form a new register closer to the TCAT loop.

complex, the RHD elements (for example, α 1, α 5, TCAT loop) do not undergo any conformational changes as the AHD progresses from open to closed conformation, but instead maintain the same position as the one observed in the nucleotide-free crystal structure (PDB 3SN6) (Fig. 3).

The switch regions (SwI–SwIII) of the G α RHD undergo conformational transitions during activation to facilitate GTP binding and target downstream effector enzymes, primarily adenylyl cyclase in the case of G α s⁷⁴². Following closure of the AHD, initial stabilization of the GTP phosphate tail and α 1 helical extension, SwI begins changing conformation to orient towards the nucleotide-binding pocket, whereas SwIII, which is not fully resolved in early intermediates, starts to order towards the nucleotide, probably due to contacts formed with the α D– α E loop of the closed AHD (Fig. 3). The short loop connecting the G α s β 2– β 3 strands, lying between the SwI and SwII regions, contains an aspartic acid residue (Asp215) that forms an ionic interaction with Arg373 on

the α 5 helix of G α in the early intermediate conformers (Fig. 3e). This interaction helps stabilize the α 5 helix in its extended conformation towards the receptor. In the later frames of the conformational trajectory, the movement of SwII correlates with the movement of the β 2– β 3 linker, in a lever-like fashion, away from the α 5 helix. This separation, in conjunction with a loss of helicity in α 5 near the TCAT motif, breaks the Asp215–Arg373 interaction and the helical register of α 5 (Fig. 3c and Supplementary Table 4), and allows for the re-formation of a new register in which α 5 begins three amino acids earlier, bringing it a helical turn closer to the TCAT motif. The change in helicity also displaces the α 5 residue Phe376, previously identified as a relay during activation⁴³, from interacting with β_2 AR Phe139^{34,51} (Ballesteros–Weinstein⁴⁴ numbering in superscript) within intracellular loop 2 (ICL2), thus losing a critical interaction with the receptor. In the new α 5 helical register, Phe376 is moved backward and protected by a hydrophobic groove of the RHD β -sheets (Extended Data Fig. 8). Most notably, except for

the most C-terminal portion of $\alpha 5$ that has not fully formed into a stable helix, the RHD elements within the final intermediate structure are strikingly similar to those observed in the crystal structure of the activated G α -GTPyS structure (PDB 1AZT)⁴⁵ (Fig. 3 and Extended Data Fig. 8). The observation that our trajectory reveals a transition series from a conformation with open AHD, in which the G protein assumes a structure like the crystal structure of G α s bound to β_2 AR (PDB 3SN6)², to a conformation with closed AHD, in which the receptor-bound G α s subunit is nearly identical to the crystal structure of the activated G protein alone (PDB 1AZT)⁴⁵ strongly supports that, within the limitations of a linear subspace fitting of our data implemented in 3DVA, these reconstruction frames reflect an appropriately ordered chain of main events leading to G-protein activation after GTP binding, as also supported by the time-dependent changes observed through traditional 3D classification. The progressive repositioning and stabilization of GTP within the binding pocket, extension and relocation of switch II and III regions towards the GTP site, an extension of the $\alpha 1$ helix, change of $\alpha 5$ helical register along with corresponding breakage of the Asp215–Arg373 interaction and destabilization of the β_2 AR density are observed in traditional 3D classification reconstructions ordered by increasing particle contribution of the 17 second dataset (Supplementary Fig. 7 and Supplementary Table 5).

Destabilization of the GPCR–G-protein interface

Also observed in the later intermediates of the cryo-EM trajectory is a decrease in observable density corresponding to the β_2 AR transmembrane (TM) helices. This may have resulted from a number of factors, such as flexibility in the interaction between receptor and G protein, increased plasticity in 7TM helices or even partial occupancy resulting from a fully dissociated complex. Our two-dimensional (2D) classification analysis of the projections contributing to the final reconstruction (intermediate 20) uniformly presented density for the receptor in detergent micelle (Extended Data Fig. 9a), suggesting that the decrease in 7TM resolvability resulted from flexibility rather than dissociation. To understand whether the observed increase in β_2 AR flexibility arose from a rigid body motion of β_2 AR or flexibility within individual 7TM helices, particles from each intermediate reconstruction were subjected to local refinement of the receptor density, producing cryo-EM maps with indicated resolutions between 3.2 Å and 4.1 Å (Fig. 2 and Extended Data Figs. 6 and 9). The local receptor reconstructions for frames 18–20 were highly similar at the secondary structure level, and, compared to earlier frames, exhibited mostly minor movements in residue side chains and a small movement of the ligand towards extracellular loop 2/TM2 within the extracellular cavity of β_2 AR. These results imply that in the late intermediates of the analysed trajectory (intermediates 18–20), the overall disappearing receptor densities are primarily due to the flexible disposition between receptor and G protein, without the receptor undergoing major conformational changes within this period.

In early cryo-EM intermediates (1–16), the $\alpha 5$ helix is fully engaged and G α forms interfaces with ICL2, TM5 and TM6 of the receptor. Phe139^{34,51} on the ICL2 of β_2 AR makes contacts with Phe362, Arg366 and Ile369 on the $\alpha 5$ helix, and with His41 on the αN – $\beta 1$ hinge loop (Fig. 4a). The immediately adjacent Pro138^{34,50} on ICL2 produces an additional $\alpha 5$ contact and participates in coordinating Phe139^{34,51}. On the other hand, TM5 makes extensive contacts with the C terminus of G α , $\alpha 5$ helix, $\alpha 4$ – $\beta 6$ loop and $\alpha 4$ helix, whereas TM6 primarily contacts the C-terminal residues of G α s. Remarkably, the majority of these interactions with the receptor are progressively lost as the AHD closes on the GTP-loaded RHD (intermediates 15–20). At the macroscopic level, as evident when all models are aligned by the receptor structure, the G-protein heterotrimer assumes small but increasing anticlockwise rotations across the receptor axis as viewed from the cytoplasm, suggesting that the pathway of G-protein disengagement from the receptor is directional (Extended Data Fig. 8). This in-plane rotation may

be important to destabilize interactions with TM5, which appears to extend its cytoplasmic helicity coincident with establishing interactions with the RHD of G α . Disengagement of G protein from β_2 AR would be a logical next step following changes at the interface of G α s and β_2 AR that occur in later intermediates (18–20), particularly given the dramatic restructuring of the G α $\alpha 5$ helix and C terminus, which form the central point of contact with ICL2, TM5 and TM6 of the receptor.

G-protein dissociation from the receptor

Given the small subunit size ((β_2 AR (52 kDa), G α s (44 kDa) or G $\beta\gamma$ (46 kDa)), in combination with conformational and compositional heterogeneity presented in these samples, it is inherently very challenging to obtain high-resolution information of dissociation products by cryo-EM. However, in the longest time point collected in the presence of GTP, we observed several 2D class averages containing a receptor micelle with an attached density of a size that could correspond to either G $\beta\gamma$ or G α s, but not both. The 3D classification using these particles resulted in low-resolution envelopes in which either G $\beta\gamma$ or G α s alone could be fitted, or density that was too ambiguous for assignment (Supplementary Fig. 4). The presence of only one G-protein component (that is, G α s or G $\beta\gamma$) density in these classes is indicative of either complete dissociation or very high flexibility of the absent subunits relative to the rest of the complex micelle. We note that these particles were not included in the curated dataset contributing to our 3DVA analysis, as they did not represent the full complex.

To further probe the structural transitions in the late steps of β_2 AR–G α _s^{GTP(Merged)}, we performed molecular dynamics (MD) simulations of intermediate frames 16–20. For this work, we docked the locally refined receptor models into the globally refined density maps to create composite models with more complete receptor information (Supplementary Table 6). Triplicate runs for each cryo-EM intermediate structure over 3 μs simulations revealed a similar, but progressive, sequence of events over the time course of the MD trajectories. GTP was positionally variable over the simulated trajectory arising from cryo-EM intermediate 16 and 17. Correspondingly, GTP stabilization through enhanced interactions within its binding site increased over the course of the simulations (Fig. 4d). In the MD trajectories starting from frames in which the ionic interaction between Asp215 on the $\beta 2$ – $\beta 3$ loop and Arg373 on $\alpha 5$ is still present (intermediate frames 16 and 17), the interaction is maintained 60–90% of the simulated time (Extended Data Fig. 10). Strikingly, however, this interaction never re-forms in the MD trajectories starting from an already broken bond (intermediate frames 18–20), indicating the propensity of the Asp215–Arg373 interaction to break in the transitional structures (frames 16 and 17), forming a barrier to complex re-forming (frames 18–20). This split of the MD data in frames 16 and 17 versus 18–20 also correlates with an observed destabilization of the interface between G protein and receptor, with a decreasing number of contacts in MD trajectories starting from intermediate frames 17 and 18 (Fig. 4 and Extended Data Fig. 10). In particular, the β_2 AR TM5 decreases contacts with the G α s $\alpha 5$ helix, $\beta 6$ strand and the loop between $\alpha 4$ and $\beta 6$, whereas the β_2 AR ICL2 loses contacts with G α s αN , αN – $\beta 1$ hinge, $\beta 1$ strand, $\beta 2$ – $\beta 3$ loop and $\beta 3$ strand (Extended Data Fig. 10). This drop in interface contacts is reflected by the enhanced mobility of the G protein relative to the receptor, which again splits sharply between MD trajectories starting from intermediate frames 16 and 17 versus 18–20 (Fig. 4c). Notably, an anticlockwise rotation of the G protein relative to the receptor when viewed from the cytoplasmic side, as also found in our cryo-EM data, was observed as a trend in our MD data (Fig. 4c and Extended Data Fig. 10), supporting the concept of a directional dissociation pathway.

Collectively, the MD simulations show that enhanced contacts with GTP on tight AHD closure correlates with G α s $\alpha 5$ helix destabilization and that the structures representing the late frames (16–20) of the cryo-EM trajectories lead to functional dissociation, an event that

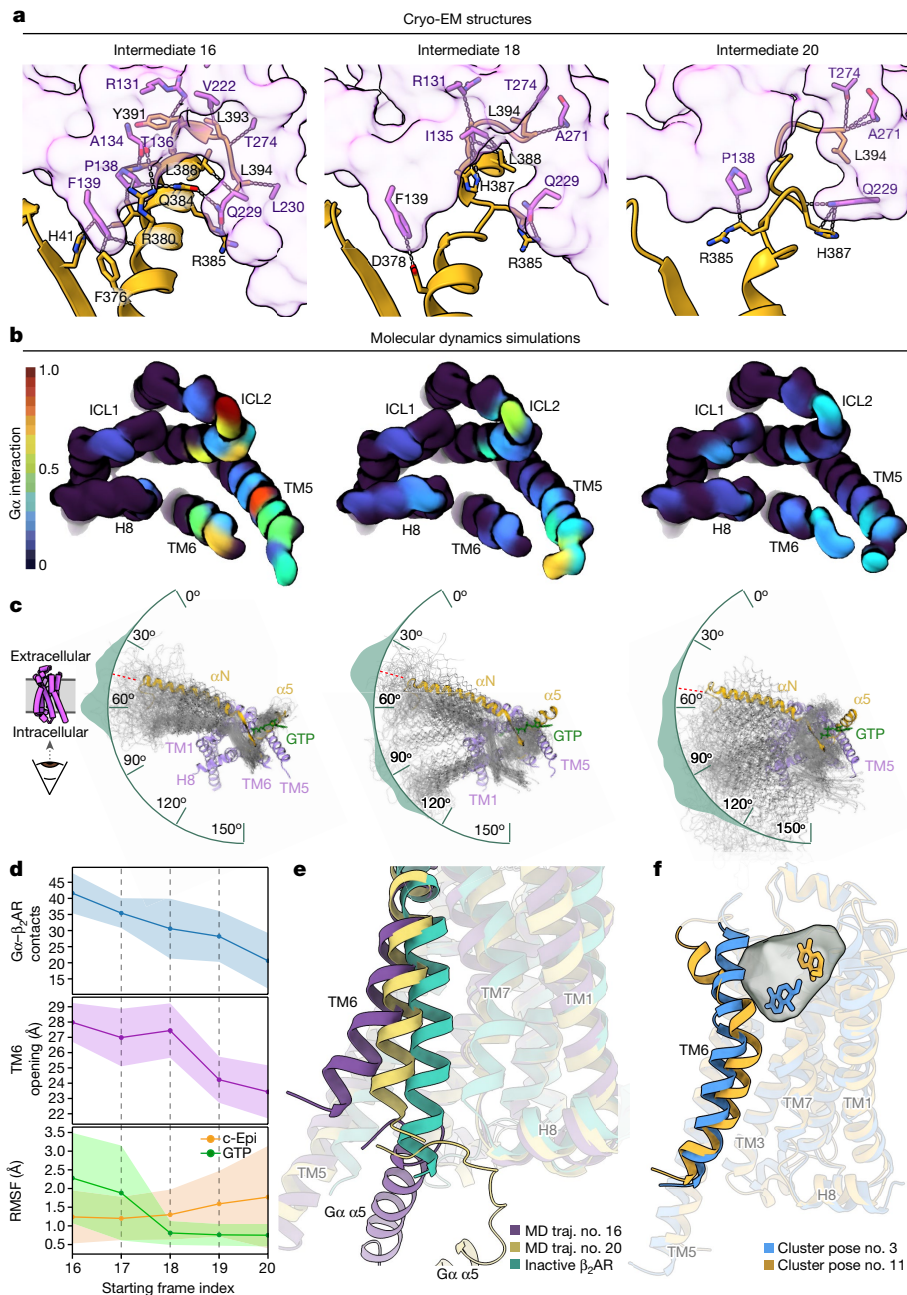


Fig. 4 | Destabilization of the β_2 AR–G_s interface. **a**, Interactions between β_2 AR and G_s decrease over the activation trajectory in the cryo-EM structures. **b, d**, MD simulations starting from the cryo-EM intermediate structures show that the sum of interactions between β_2 AR and G_s over the MD trajectories decrease with starting structures from later cryo-EM frames, particularly at ICL2 and TM5 (see also panel **d** and Extended Data Fig. 10a). **c**, The decrease in β_2 AR–G_s interaction coincides with directional flexibility of the G protein in relation to the receptor. MD models were aligned to β_2 AR, the initial structures for each trajectory are shown in full colour with resulting periodic trajectory snapshots overlaid in grey. Encompassing each overlay is the distribution of angles of the G_s in relation to β_2 AR over the MD trajectories. The initial angle is indicated by a red dashed line. Panels **b** and **c** are shown as viewed from the cytoplasmic space. **d**, Quantification of G_s- β_2 AR contacts (top), TM6 opening (middle) and mobility of GTP and c-Epi (bottom) over the MD trajectories started from sequential frames 16–20. The backdrop band in faint colour represents the approximate

95% confidence interval (two standard deviations) assuming a normal distribution of values. **e**, TM6 is found in a semi-closed conformation in simulations starting from late cryo-EM frames. Shown are the representative structures from MD simulations started from cryo-EM intermediates 16 (purple) and 20 (yellow) superimposed with inactive β_2 AR (green) (PDB 2RH1)⁴⁷. TM6 and the G_s C terminus and α5 helix are shown in full colour. **f**, Two representative ligand poses showing the ligand dynamics captured in the MD trajectories. The grey cloud shows the space sampled by the ligand during the simulations (Extended Data Fig. 10j, Supplementary Table 6 and Supplementary Video 11). The blue model represents the ligand pose (no. 3) that is most abundant in trajectories started from earlier intermediate frames, whereas the orange represents a pose (no. 11) that develops in MD trajectories started from cryo-EM intermediate 20. The extracellular half of TM7 has been hidden to show the ligand site. TM6 is shown in full colour.

becomes increasingly irreversible on the initial destabilization of receptor–G-protein interactions. In one trajectory started from frame 20 we observed near-complete detachment of the G protein from the receptor,

beginning with loss of interaction between ICL2 and the α5 helix. This coincides with α5 unravelling, as we also observed by cryo-EM, initially maintaining C-terminal contacts with the TM5–ICL3–TM6 region, but

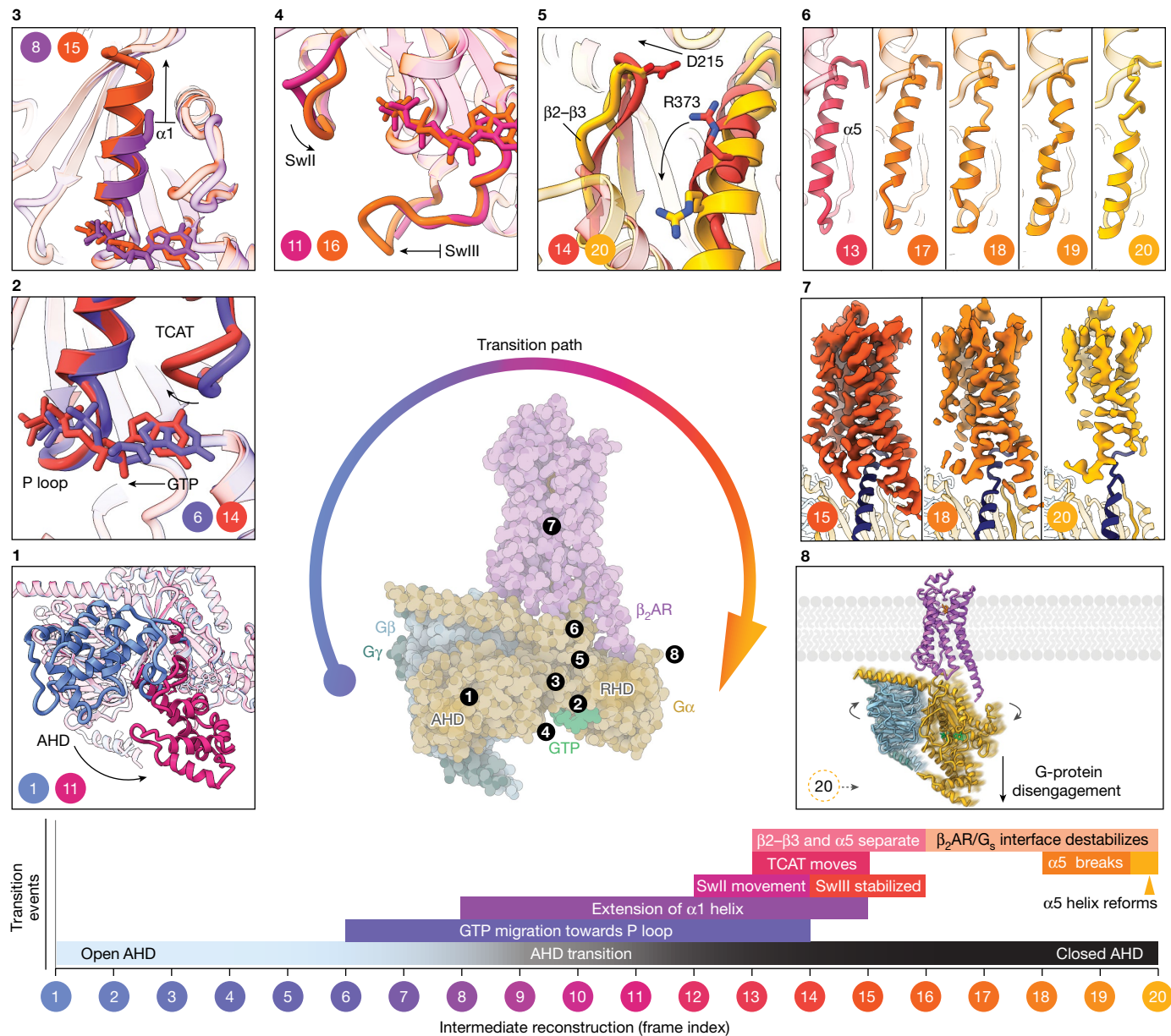


Fig. 5 | Stepwise activation of G protein following nucleotide exchange initiated by a GPCR. Progression of G-protein activation through transitional events over the course of the 20 cryo-EM structures indicated from 1 to 20 from shades of blue to pink to yellow. Boxed, clockwise from the lower left: closure of the AHD against the RHD; stabilization of GTP towards the P loop and corresponding movement of the TCAT motif; extension of the $\alpha 1$ helix;

movement of switch II towards GTP and stabilization of switch III; distancing of $\beta 2-\beta 3$ from $\alpha 5$ and breakage of ionic lock; breakage and re-formation of the $\alpha 5$ helix into new register beginning closer to the TCAT motif; destabilization of the receptor–G-protein complex; disengagement of the G protein from the receptor. Shown in the lower panel is the relative timeline of overlapping events occurring over the cryo-EM trajectory.

eventually losing interactions with the receptor core. In MD trajectories started from the structures of the latest frames (19 and 20), the gradual disengagement of the G protein correlates with the transition of the cytoplasmic half of TM6 towards a closed conformation, a trademark of GPCR inactivation that reduces the accessibility of the intracellular receptor cavity to G proteins or arrestin^{46,47} (Fig. 4d,e). In a lever-like fashion, the inward movement on the intracellular side of TM6 results in an outward movement of its extracellular side (Fig. 4d,e and Extended Data Fig. 10), which correlates with increased mobility of the ligand c-Epi within the ligand-binding cavity (Fig. 4f and Extended Data Fig. 10). Characteristically, c-Epi tends to migrate towards the putative entry channel and the extracellular vestibule associated with ligand entry⁴⁸. These results, which reflect the allosteric communication between the extracellular ligand-binding pocket and the intracellular G-protein

binding cavity^{46,49}, further reinforce the validity of our findings and suggest that the TM6 of β_2 AR approaches a conformation similar to the inactive state relatively swiftly after functional dissociation of the activated G protein.

Stepwise mechanism of G-protein activation by GTP loading

Our time-resolved cryo-EM structures highlight a sequential series of structural transitions underlying G-protein activation following GTP loading (Fig. 5). These conformational changes can be broadly classified into early-, intermediate- and late-phase events. Initial GTP binding is coordinated by interactions with the TCAT and P loop of G α , which change their conformation compared to the nucleotide-free G protein.

During early-phase events, the AHD is in an open conformation away from the RHD enabling initial binding of GTP. In this phase, the bound GTP may gradually increase its number of contacts with the P loop and TCAT but without any long-range effects on the rest of the RHD. Marking the beginning of intermediate events is the transition of the flexible AHD towards a closed conformation. Unlike the nucleotide-free G protein, the AHD in a closed conformation becomes well ordered in this state through further interactions with the nucleotide, which essentially bridges the interface between the AHD and RHD. The locking of AHD against the GTP is a watershed event, initiating intermediate-phase events involving Gα rearrangements. During this phase, we observe the helical extension of the α1 helix, presumably due to both the increased coordination of the P loop by the phosphate tails of GTP and the AHD ordering that connects directly to the α1 via a linker region. We also observe a conformational change in SwI, which comes closer to the γ-phosphate. These events also coincide with the full ordering of the dynamic SwIII towards the nucleotide. The tight stabilization of GTP by the backbone amine of P-loop residues Glu50, Ser51 and Gly52; α1 helix residues Lys53, Ser54 and Thr55; and SwI region Arg201 further stabilizes GTP within the nucleotide-binding pocket. The stabilized nucleotide also acts to bridge the AHD and RHD through an interaction of Lys293^{RHD} with both the purine ring of GTP and Asp173 of the AHD, whereas Glu50 and the phosphate tail of GTP interact with Arg201 of the AHD. This full set of GTP interactions marks the beginning of the late-phase events in the activation process.

Late-phase events involve long-range effects of GTP binding, with the hallmark of profound structural rearrangements of the α5 helix. These include the unravelling, breaking and re-formation of α5 with a different helical register. Our intermediate frames indicate that Asp215, positioned in the β2–β3 loop, pulls away from Arg373 in α5 due to the interactions of the SwI and SwII loops, flanking β2 and β3, with GTP. The weakening of the Asp215–Arg373 electrostatic interaction appears to enable the partial unravelling of the N-terminal end of α5, probably also due to the strain from the tighter interactions established by the associated TCAT motif with GTP. This enables the re-formation of a small helical segment close to the TCAT that appears to grow while helix α5 breaks, with extensive unravelling of the C terminus. The break enables the re-formation of α5 with a new register that starts from the helical segment close to the TCAT motif. The destabilization of the ‘nucleotide-free’ conformation of α5 and loss of helical structure at the Gα C terminus is detrimental to the stability of the interface with the receptor. Late-phase intermediate frames of the cryo-EM trajectory show the deterioration of features in receptor density, the result of flexibility at their interface. The last frame in our reconstruction series reveals no secondary structure at the Gα C terminus, which has entirely unravelled, giving the impression that the G protein is almost hanging on to the receptor by ‘a thread’. Given the tenuous interactions, we assume that the next step would be the functional dissociation of the G protein, as also fully supported by our MD simulations (Extended Data Fig. 10 and Supplementary Video 11). Of note, the structure of the Gα C terminus in the final cryo-EM frame is highly reminiscent of a transition intermediate we previously captured in the cryo-EM structure of the viral GPCR US28 in complex with G11 (PDB 7RKF)⁵⁰, in which GDP is not yet released and the C terminus of α5 is unravelled proximal to the receptor (Extended Data Fig. 8j–k). This observation supports the notion that the G protein undergoes similar transitions in reverse order to release GDP on initial association with the receptor.

Discussion

We developed a time-resolved approach to visualize dynamic events driving G-protein activation and receptor disengagement following GTP binding to a nucleotide-free GPCR–G-protein complex. The conformational changes observed in 20 transition cryo-EM structures of pre-steady-state β₂AR–G_s^{GTP} compared to the corresponding analysis

of β₂AR–G_s^{EMPTY} suggest that G-protein dissociation driven by GTP binding is underlined by ordered structural changes propagating from the nucleotide-binding site and extending to the receptor interface, weakening the interactions between the GPCR and the G protein. Progressive stabilization of the nucleotide between the RHD and AHD correlates with the structural rearrangement of the Gα5 helix, resulting in destabilization of the receptor interface and the beginning of G-protein dissociation, trends which were also observed in MD simulations. In many ways this process appears to be the inverse to the process of GPCR–G-protein association, in which the α5 helix must rearrange outwards to engage the intracellular cavity of the receptor, with parallel ejection of GDP. In support of the equivalent conformational pathways involving G-protein association and dissociation, a separate MD study examining β₂AR–G_s protein association⁵¹ found that the process involves an in-plane rotation of the G protein against the receptor in the opposite direction to the one we observe here for dissociation. Thus, a corkscrew binding and unbinding pattern appears to underline G-protein nucleotide exchange by GPCRs.

The implementation of freeze trapping at different time points enabled us to monitor the progression of conformational ensembles and confirm our interpretation and ordering of events. For this work, we used standard equipment to vitrify samples within seconds after initiating a ‘reaction’ at 4 °C, which was sufficient to monitor and reconstruct a meaningful structural ensemble for the question at hand. However, different kinds of questions or types of complexes may necessitate specialized instrumentation or approaches that can monitor faster kinetics with cryo-EM, including ligand spraying⁵², microfluidic mixing and spraying on grids, as has been demonstrated with ribosomes^{53–55}, and also rapid release of caged ligands through laser pulses^{56,57}. Likewise, although we found cryoSPARC 3DVA to be suitable for our system, such projects will benefit from a rapidly advancing suite of additional processing tools, such as cryoSPARC 3DFlex⁵⁸, RELION multibody⁵⁹, cryoDRGN VAE⁶⁰ and ManifoldEM^{61,62}, to delineate structurally continuous subpopulations among heterogeneous samples.

Beyond providing an enriched mechanistic understanding of G-protein activation, we hope that this study provides a powerful demonstration for the orthogonal combination of time-resolved cryo-EM and MD simulations, which can now sample complex structural transitions in realistic computational timescales by starting with cryo-EM structures of pre-steady-state conformations. We anticipate that the structural models generated in this and future work will be a valuable resource for developing molecular dynamics simulations using several ‘checkpoint structures’, and further combined with machine learning approaches for understanding the structural dynamics of GPCR signalling.

Online content

Any methods, additional references, Nature Portfolio reporting summaries, source data, extended data, supplementary information, acknowledgements, peer review information; details of author contributions and competing interests; and statements of data and code availability are available at <https://doi.org/10.1038/s41586-024-07153-1>.

1. Cassel, D. & Selinger, Z. Catecholamine-stimulated GTPase activity in turkey erythrocyte membranes. *Biochim. Biophys. Acta* **452**, 538–551 (1976).
2. Rasmussen, S. G. et al. Crystal structure of the β₂ adrenergic receptor–G_s protein complex. *Nature* **477**, 549–555 (2011).
3. Noel, J. P., Hamm, H. E. & Sigler, P. B. The 2.2 Å crystal structure of transducin-α complexed with GTP. *S. Nature* **366**, 654–663 (1993).
4. Van Eps, N. et al. Interaction of a G protein with an activated receptor opens the interdomain interface in the alpha subunit. *Proc. Natl. Acad. Sci. USA* **108**, 9420–9424 (2011).
5. Bornancin, F., Pfister, C. & Chabre, M. The transitory complex between photoexcited rhodopsin and transducin. *Eur. J. Biochem.* **184**, 687–698 (1989).
6. Westfield, G. H. et al. Structural flexibility of the Gα5 α-helical domain in the β₂-adrenoceptor G_s complex. *Proc. Natl. Acad. Sci. USA* **108**, 16086–16091 (2011).
7. Coleman, D. et al. Structures of active conformations of G_{αi1} and the mechanism of GTP hydrolysis. *Science* **265**, 1405–1412 (1994).

- Namkung, Y. et al. Functional selectivity profiling of the angiotensin II type 1 receptor using pathway-wide BRET signaling sensors. *Sci. Signal.* <https://doi.org/10.1126/scisignal.aat1631> (2018).
- Bunemann, M., Frank, M. & Lohse, M. J. Gi protein activation in intact cells involves subunit rearrangement rather than dissociation. *Proc. Natl Acad. Sci. USA* **100**, 16077–16082 (2003).
- Manglik, A. et al. Structural insights into the dynamic process of β_2 -adrenergic receptor signaling. *Cell* **161**, 1101–1111 (2015).
- Liu, X. et al. Structural insights into the process of GPCR–G protein complex formation. *Cell* **177**, 1243–1251.e12 (2019).
- Ma, X. et al. Analysis of β 2AR-G_a and β 2AR-G_i complex formation by NMR spectroscopy. *Proc. Natl Acad. Sci. USA* **117**, 23096–23105 (2020).
- Oldham, W. M., Van Eps, N., Preiningier, A. M., Hubbell, W. L. & Hamm, H. E. Mechanism of the receptor-catalyzed activation of heterotrimeric G proteins. *Nat. Struct. Mol. Biol.* **13**, 772–777 (2006).
- Lambright, D. G., Noel, J. P., Hamm, H. E. & Sigler, P. B. Structural determinants for activation of the α -subunit of a heterotrimeric G protein. *Nature* **369**, 621–628 (1994).
- García-Nafria, J. & Tate, C. G. Structure determination of GPCRs: cryo-EM compared with X-ray crystallography. *Biochem. Soc. Trans.* **49**, 2345–2355 (2021).
- Isberg, V. et al. GPCRdb: an information system for G protein-coupled receptors. *Nucleic Acids Res.* **44**, D356–D364 (2016).
- Pandy-Székely, G. et al. GPCRdb in 2018: adding GPCR structure models and ligands. *Nucleic Acids Res.* **46**, D440–D446 (2018).
- Manglik, A., Kobilka, B. K. & Steyaert, J. Nanobodies to study G protein-coupled receptor structure and function. *Annu. Rev. Pharmacol. Toxicol.* **57**, 19–37 (2017).
- Jang, W., Lu, S., Xu, X., Wu, G. & Lambert, N. A. The role of G protein conformation in receptor–G protein selectivity. *Nat. Chem. Biol.* <https://doi.org/10.1038/s41589-022-01231-z> (2023).
- Qu, Q. et al. Insights into distinct signaling profiles of the μ OR activated by diverse agonists. *Nat. Chem. Biol.* <https://doi.org/10.1038/s41589-022-01208-y> (2022).
- Ross, E. M., Maguire, M. E., Sturgill, T. W., Biltonen, R. L. & Gilman, A. G. Relationship between the β -adrenergic receptor and adenylyl cyclase. *J. Biol. Chem.* **252**, 5761–5775 (1977).
- Robison, G. A., Butcher, R. W. & Sutherland, E. W. Cyclic AMP. *Annu. Rev. Biochem.* **37**, 149–174 (1968).
- Torphy, T. J. β -Adrenoceptors, cAMP and airway smooth muscle relaxation: challenges to the dogma. *Trends Pharmacol. Sci.* **15**, 370–374 (1994).
- Hall, I. P. in *Encyclopedia of Respiratory Medicine* (eds Laurent, G. J. & Shapiro, S. D.) 288–292 (Academic, 2006).
- Lerch, M. T. et al. Viewing rare conformations of the β_2 adrenergic receptor with pressure-resolved DEER spectroscopy. *Proc. Natl Acad. Sci. USA* **117**, 31824–31831 (2020).
- De Leán, A., Stadel, J. M. & Lefkowitz, R. J. A ternary complex model explains the agonist-specific binding properties of the adenylyl cyclase-coupled β -adrenergic receptor. *J. Biol. Chem.* **255**, 7108–7117 (1980).
- Wallukat, G. The β -adrenergic receptors. *Herz* **27**, 683–690 (2002).
- Xu, X. et al. Constrained catecholamines gain β_2 AR selectivity through allosteric effects on pocket dynamics. *Nat. Commun.* **14**, 2138 (2023).
- Punjani, A. & Fleet, D. J. 3D variability analysis: resolving continuous flexibility and discrete heterogeneity from single particle cryo-EM. *J. Struct. Biol.* **213**, 10770 (2021).
- Zhang, M. et al. Cryo-EM structure of an activated GPCR–G protein complex in lipid nanodiscs. *Nat. Struct. Mol. Biol.* **28**, 258–267 (2021).
- Traut, T. W. Physiological concentrations of purines and pyrimidines. *Mol. Cell. Biochem.* **140**, 1–22 (1994).
- Hein, P. et al. G_a activation is time-limiting in initiating receptor-mediated signaling. *J. Biol. Chem.* **281**, 33345–33351 (2006).
- Gales, C. et al. Real-time monitoring of receptor and G-protein interactions in living cells. *Nat. Methods* **2**, 177–184 (2005).
- Gregorio, G. G. et al. Single-molecule analysis of ligand efficacy in β_2 AR–G-protein activation. *Nature* **547**, 68–73 (2017).
- Markby, D. W., Onrust, R. & Bourne, H. R. Separate GTP binding and GTPase activating domains of a Gα subunit. *Science* **262**, 1895–1901 (1993).
- Carpenter, B. & Tate, C. G. Engineering a minimal G protein to facilitate crystallisation of G protein-coupled receptors in their active conformation. *Protein Eng. Des. Sel.* **29**, 583–594 (2016).
- Wan, Q. et al. Mini G protein probes for active G protein-coupled receptors (GPCRs) in live cells. *J. Biol. Chem.* **293**, 7466–7473 (2018).
- Bourne, H. R., Sanders, D. A. & McCormick, F. The GTPase superfamily: conserved structure and molecular mechanism. *Nature* **349**, 117–127 (1991).
- Graziano, M. P., Freissmuth, M. & Gilman, A. G. Expression of G_{αo} in *Escherichia coli*. Purification and properties of two forms of the protein. *J. Biol. Chem.* **264**, 409–418 (1989).
- Jones, J. C., Jones, A. M., Temple, B. R. & Dohlman, H. G. Differences in intradomain and interdomain motion confer distinct activation properties to structurally similar Gα proteins. *Proc. Natl Acad. Sci. USA* **109**, 7275–7279 (2012).
- Walker, J. E., Saraste, M., Runswick, M. J. & Gay, N. J. Distantly related sequences in the alpha- and beta-subunits of ATP synthase, myosin, kinases and other ATP-requiring enzymes and a common nucleotide binding fold. *EMBO J.* **1**, 945–951 (1982).
- Mixon, M. B. et al. Tertiary and quaternary structural changes in G_{αi1} induced by GTP hydrolysis. *Science* **270**, 954–960 (1995).
- Kaya, A. I. et al. A conserved phenylalanine as a relay between the a5 helix and the GDP binding region of heterotrimeric G_i protein α subunit. *J. Biol. Chem.* **289**, 24475–24487 (2014).
- Ballesteros, J. A. & Weinstein, H. in *Methods in Neurosciences Vol. 25* (ed. Sealoff, S. C.) 366–428 (Academic, 1995).
- Sunahara, R. K., Tesmer, J. J., Gilman, A. G. & Sprang, S. R. Crystal structure of the adenylyl cyclase activator G_{αo}. *Science* **278**, 1943–1947 (1997).
- Nygaard, R. et al. The dynamic process of β_2 -adrenergic receptor activation. *Cell* **152**, 532–542 (2013).
- Cherezov, V. et al. High-resolution crystal structure of an engineered human β_2 -adrenergic G protein-coupled receptor. *Science* **318**, 1258–1265 (2007).
- Dror, R. O. et al. Pathway and mechanism of drug binding to G-protein-coupled receptors. *Proc. Natl Acad. Sci. USA* **108**, 13118–13123 (2011).
- DeVree, B. T. et al. Allosteric coupling from G protein to the agonist-binding pocket in GPCRs. *Nature* **535**, 182–186 (2016).
- Tsutsumi, N. et al. Atypical structural snapshots of human cytomegalovirus GPCR interactions with host G proteins. *Sci. Adv.* **8**, eab15442 (2022).
- Batebi, H. et al. Mechanistic insights into G protein association with a G protein-coupled receptor. Preprint at Research Square <https://doi.org/10.21203/rs.3.rs-2851358/v1> (2023).
- Berriman, J. & Unwin, N. Analysis of transient structures by cryo-microscopy combined with rapid mixing of spray droplets. *Ultramicroscopy* **56**, 241–252 (1994).
- Chen, B. et al. Structural dynamics of ribosome subunit association studied by mixing-spraying time-resolved cryogenic electron microscopy. *Structure* **23**, 1097–1105 (2015).
- Kaledhonkar, S., Fu, Z., White, H. & Frank, J. Time-resolved cryo-electron microscopy using a microfluidic chip. *Methods Mol. Biol.* **1764**, 59–71 (2018).
- Feng, X. et al. A fast and effective microfluidic spraying-plunging method for high-resolution single-particle cryo-EM. *Structure* **25**, 663–670.e663 (2017).
- Ménétret, J. F., Hofmann, W., Schröder, R. R., Rapp, G. & Goody, R. S. Time-resolved cryo-electron microscopic study of the dissociation of actomyosin induced by photolysis of photolabile nucleotides. *J. Mol. Biol.* **219**, 139–144 (1991).
- Yoder, N. et al. Light-coupled cryo-plunger for time-resolved cryo-EM. *J. Struct. Biol.* **212**, 107624 (2020).
- Punjani, A. & Fleet, D. 3D flexible refinement: structure and motion of flexible proteins from cryo-EM. *Microsc. Microanal.* **28**, 1218–1218 (2022).
- Nakane, T., Kimanis, D., Lindahl, E. & Scheres, S. H. W. Characterisation of molecular motions in cryo-EM single-particle data by multi-body refinement in RELION. *eLife* **7**, e36861 (2018).
- Zhong, E. D., Bepler, T., Berger, B. & Davis, J. H. CryoDRGN: reconstruction of heterogeneous cryo-EM structures using neural networks. *Nat. Methods* **18**, 176–185 (2021).
- Frank, J. & Ourmazd, A. Continuous changes in structure mapped by manifold embedding of single-particle data in cryo-EM. *Methods* **100**, 61–67 (2016).
- Dashти, A. et al. Retrieving functional pathways of biomolecules from single-particle snapshots. *Nat. Commun.* **11**, 4734 (2020).

Publisher's note Springer Nature remains neutral with regard to jurisdictional claims in published maps and institutional affiliations.

Springer Nature or its licensor (e.g. a society or other partner) holds exclusive rights to this article under a publishing agreement with the author(s) or other rightsholder(s); author self-archiving of the accepted manuscript version of this article is solely governed by the terms of such publishing agreement and applicable law.

© The Author(s), under exclusive licence to Springer Nature Limited 2024

Methods

Expression and purification of the β_2 AR for complex formation
 β_2 AR was expressed and purified as previously described². Briefly, *Spodoptera frugiperda* (Sf9) insect cells (unauthenticated and untested for mycoplasma contamination, Expression Systems) were infected with recombinant baculovirus (BestBac Expression Systems) at a density of about 4.0×10^6 cells per ml. The cells were collected 55 h post-infection and lysed by osmotic shock, followed by solubilization of the receptor in *n*-dodecyl- β -D-maltoside (DDM). The soluble fraction was loaded on an M1 anti-FLAG immunoaffinity chromatograph as the initial purification step, followed by alprenolol-sepharose chromatography (alprenolol-sepharose resin prepared in-house) to isolate only functional receptors. The eluted receptor was subsequently concentrated on M1 FLAG affinity resin and then washed with ligand-free buffer for 1 h at room temperature to eliminate the bound orthosteric ligand alprenolol. After elution of the ligand-free receptor with 20 mM HEPES pH 7.5, 350 mM NaCl, 0.1% DDM, 0.01% cholesteryl hemisuccinate (CHS), 5 mM ethylenediaminetetraacetic acid (EDTA) and 0.2 mg ml⁻¹ FLAG peptide, the protein was concentrated in a 100 kDa MWCO Amicon spin concentrator and further purified by size-exclusion chromatography on a Superdex200 Increase 10/300GL (Cytiva) gel filtration column in buffer containing 20 mM HEPES pH 7.5, 100 mM NaCl, 0.05% DDM, and 0.005% CHS. The monodisperse peak of the receptor was pooled and concentrated to approximately 250 μ M for further complexing with agonist and G-protein heterotrimer.

Expression and purification of the heterotrimeric G protein G_s
 G_s Heterotrimeric G_s was expressed and purified as previously described⁶³. Briefly, *Trichoplusia ni* (*T. ni*) insect cells (unauthenticated and untested for mycoplasma contamination, Expression Systems) were co-infected with two baculoviruses at a density of about 3.0×10^6 cells per ml, one encoding the human $G_{\alpha}s$ -short splice variant and the other encoding both the $G_{\beta}1$ and $G_{\gamma}2$ subunits, with a histidine tag (6×His) and HRV 3C protease site inserted at the amino terminus of the β -subunit. Cells were collected 48 h postinfection by centrifugation and lysed in a buffer consisting of 10 mM Tris, pH 7.5, 100 μ M MgCl₂, 5 mM β -mercaptoethanol (β -ME), 20 μ M GDP and protease inhibitors. The membrane fraction was collected by centrifugation solubilized with a buffer consisting of 20 mM HEPES pH 7.5, 100 mM sodium chloride, 1% sodium cholate, 0.05% DDM, 5 mM magnesium chloride, 5 mM β -ME, 5 mM imidazole, 20 μ M GDP and protease inhibitors. The soluble fraction was purified using Ni-chelating sepharose chromatography, and the detergent was gradually exchanged from cholate/DDM mixture to 0.1% DDM. The protein was eluted in buffer supplemented with 200 mM imidazole, pooled and HRV 3C protease was added to cleave the N-terminal 6×His tag during overnight dialysis in 20 mM HEPES pH 7.5, 100 mM sodium chloride, 0.1% DDM, 1 mM magnesium chloride, 5 mM β -ME and 20 μ M GDP. The cleaved 6×His tag, uncleaved fractions and 3C protease were removed by a reverse Ni-chelated sepharose step. The unbound fraction was dephosphorylated using lambda protein phosphatase (NEB), calf intestinal phosphatase (NEB) and Antarctic phosphatase (NEB) in the presence of 1 mM manganese chloride at 4 °C for 1 h. Fully geranylgeranylated G_s heterotrimer was isolated using a MonoQ10/100 GL column (GE Healthcare). After binding the protein to the column in buffer A (20 mM HEPES (pH 7.5), 50 mM sodium chloride, 1 mM MgCl₂, 0.05% DDM, 100 μ M TCEP and 20 μ M GDP), the column was washed with buffer A and the G-protein heterotrimer was eluted with a linear gradient of 0–50% buffer B (buffer A containing 1 M sodium chloride). The main peak containing isoprenylated G-protein heterotrimer was collected and the protein was dialysed into 20 mM HEPES pH 7.5, 100 mM sodium chloride, 0.02% DDM, 100 μ M TCEP and 20 μ M GDP. After concentrating the protein to approximately 250 μ M, glycerol was added to a final concentration of 20%, and the protein was flash frozen in liquid nitrogen and stored at -80 °C until further use.

Chemical synthesis of c-Epi

5,6-Dimethoxy-3,4-dihydronaphthalen-1(2H)-one (1.90 g, 9.21 mmol) was dissolved in dry toluene (100 ml), which was degassed with N₂ for 15 min. To the solution was added AlCl₃ (6.14 g, 46.1 mmol). The mixture was heated to reflux for 1 h and subsequently cooled on ice. Then, water (30 ml) and 2 M HCl (30 ml) were sequentially added. The precipitate was collected by filtration and washed with water (30 ml). The solid was dried under vacuum to give pure 5,6-dihydroxy-3,4-dihydronaphthalen-1(2H)-one as a pale brown solid (1.15 g, 70%).

Benzyl bromide (2.30 ml, 19.4 mmol) was dissolved in acetone (80 ml) and NaI (2.13 g, 14.2 mmol) was added. After stirring at room temperature for 15 min, K₂CO₃ was added (4.46 g, 32.3 mmol), followed by addition of 5,6-dihydroxy-3,4-dihydronaphthalen-1(2H)-one (1.15 g, 6.45 mmol). The mixture was heated to reflux for 2 h. Water (100 ml) was added, the product was extracted with EtOAc (3 × 50 ml) and the combined layers were washed with brine, dried (Na₂SO₄) and evaporated. The residue was purified by recrystallization from methanol (40 ml), and residual mother liquor was purified by flash column chromatography (4:1 *n*-hexane/EtOAc) to give 5,6-bis(benzylxy)-3,4-dihydronaphthalen-1(2H)-one as a solid (2.09 g, 90%).

5,6-Bis(benzylxy)-3,4-dihydronaphthalen-1(2H)-one (410 mg, 1.14 mmol) was dissolved in Et₂O (20 ml) and a solution of bromine (117 μ l, 2.29 mmol) in Et₂O (10 ml) was added to the stirred solution. After 1 h, 50% NaHCO₃ solution (20 ml) was slowly added, and the product was extracted with further Et₂O (2 × 20 ml). The combined organic layers were washed with Na₂S₂O₃ (10% aqueous solution, 30 ml), brine, dried with Na₂SO₄ and concentrated in vacuo to give a mixture of the mono- and α,α -dibromo compounds. The crude product was dissolved in dry THF (10 ml) and cooled on ice. To this solution was added dropwise a solution of triethyl amine (167 μ l, 1.20 mmol) and diethyl phosphite (154 μ l, 1.20 mmol) in THF (10 ml) over a period of 10 min. After stirring for 16 h, water (20 ml) was added, and the product was extracted with EtOAc (2 × 20 ml). The combined organic layers were washed with brine, dried (Na₂SO₄), concentrated and the residue was purified by flash column chromatography (5:1 *n*-hexane/EtOAc) to give 5,6-bis(benzylxy)-2-bromo-3,4-dihydronaphthalen-1(2H)-one as a yellow oil (485 mg, 97%).

5,6-Bis(benzylxy)-2-bromo-3,4-dihydronaphthalen-1(2H)-one (1.44 g, 3.29 mmol) was dissolved in DMF (50 ml) and cooled on ice. To the stirred solution was added glacial acetic acid (226 μ l, 3.95 mmol), then after 5 min a solution of sodium azide (428 mg, 6.59 mmol) in water (3 ml) was added. After 3 h stirring at 0 °C, water (50 ml) was added, followed by CH₂Cl₂ (40 ml) and the product was extracted with further CH₂Cl₂ (2 × 30 ml). The combined organic layers were washed with brine, dried (MgSO₄) and concentrated in vacuo. The oil was then dissolved in Et₂O (30 ml) and the solution was washed with water (3 × 50 ml), brine, dried (Na₂SO₄) and evaporated to crude 2-azido-5,6-bis(benzylxy)-3,4-dihydronaphthalen-1(2H)-one (1.22 g, 93%), which could be used immediately for the next reaction step.

2-Azido-5,6-bis(benzylxy)-3,4-dihydronaphthalen-1(2H)-one (550 mg, 1.38 mmol) was dissolved in 1,2-DCE (20 ml) and LiAlH₄ (1 M solution in THF, 4.13 ml, 4.13 mmol) was added over a period of 1 h. After 4 h, the reaction was cooled on ice and quenched with water (30 ml). The mixture was further diluted with CH₂Cl₂ (50 ml), then filtered to remove solids. The product was further extracted with CH₂Cl₂ (3 × 30 ml), and the combined organic layers were washed with brine, dried (Na₂SO₄) and concentrated to give 2-amino-5,6-bis(benzylxy)-1,2,3,4-tetrahydronaphthalen-1-ol as a yellow oil (485 mg, 94%), in approximately 2:3 *cis/trans* ratio.

2-Amino-5,6-bis(benzylxy)-1,2,3,4-tetrahydronaphthalen-1-ol, *cis/trans* mixture (4.00 g, 10.6 mmol, approx. 70% *trans*) was dissolved in anhydrous CH₂Cl₂ (100 ml). After addition of *N,N*-diisopropylethylamine (3.62 ml, 21.3 mmol), Boc₂O (4.65 g, 21.3 mmol) was added under a stream of nitrogen and the reaction mixture was thereafter stirred

Article

overnight (18 h). It was evaporated and the residue was purified by flash column chromatography (isohexane/acetone 5:1 to 2:1), yielding *tert*-butyl-((1*S,2R*)-5,6-bis(benzyloxy)-1-hydroxy-1,2,3,4-tetrahydronaphthalen-2-yl)carbamate enriched with the *trans* isomers (greater than 90%). After recrystallization of the beige-pink solid (toluene/isohexane, 2:1), a white, diastereomerically pure powder was obtained (3.01 g, 60% yield). Small amounts of *trans* compound can be separated on chiral, preparative HPLC (ChiralPak IC) with acetonitrile as eluent, giving first the (*R,R*)- and second the (*S,S*)-enantiomer.

To a solution of *tert*-butyl-((1*S,2R*)-5,6-bis(benzyloxy)-1-hydroxy-1,2,3,4-tetrahydronaphthalen-2-yl)carbamate (7.00 g, 14.7 mmol) in absolute CH₂Cl₂ (150 ml) was added 2–3 drops of dibutyltin dilaurate and subsequently (*R*)-methylbenzyl isocyanate (2.49 ml, 17.7 mmol, enantiomeric excess greater than 98%). The clear solution was stirred under nitrogen atmosphere at room temperature for 7 d. It was quenched with 2 M NaOH solution (50 ml, stirring for 30 min), the organic layer was separated and the aqueous layer was extracted again with CH₂Cl₂. The pooled, organic fractions were washed with water (2×), dried (MgSO₄) and evaporated, to give a beige powder in quantitative yield. The crude mixture of *tert*-butyl-((1*R,2R*)-5,6-bis(benzyloxy)-1-(((*R*)-1-phenylethyl)carbamoyl)oxy)-1,2,3,4-tetrahydronaphthalen-2-yl)carbamate was recrystallized from toluene/isohexane (1:1), enabling the hot and clear solution to cool down slowly over the course of several hours. After complete precipitation, the white powder was filtered under vacuum, washed with isohexane/toluene (4:1), followed by pure isohexane, yielding a residue consisting of 90% (*R,R,R*)-isomer (5.47 g). After a second recrystallization (toluene/isohexane (5:1), approximately 240 ml of solvent), analytically pure (*R,R,R*)-compound was obtained as a white powder (3.90 g, 85%, yield calculated for single diastereomer).

To a solution of *tert*-butyl-((1*R,2R*)-5,6-bis(benzyloxy)-1-(((*R*)-1-phenylethyl)carbamoyl)oxy)-1,2,3,4-tetrahydronaphthalen-2-yl)carbamate (60 mg, 0.096 mmol) in THF (2 ml) was added 4 M LiAlH₄ solution in Et₂O (145 µl, 0.58 mmol, 6 equiv.) and the resulting reaction mixture was heated to 85 °C for 1 h. After careful addition of water and extraction with CH₂Cl₂ (3×), the combined organic layers were washed with brine, dried over MgSO₄ and evaporated. The resulting crude solid was purified by flash column chromatography (gradient, CH₂Cl₂ to CH₂Cl₂/MeOH 9:1) to yield (1*R,2R*)-5,6-bis(benzyloxy)-2-(methylamino)-1,2,3,4-tetrahydronaphthalen-1-ol as a beige powder (23.1 mg, 62% yield).

To a solution of (1*R,2R*)-5,6-bis(benzyloxy)-2-(methylamino)-1,2,3,4-tetrahydronaphthalen-1-ol (230 mg, 0.59 mmol) in ethanol (15 ml) was added 10% Pd/C (23.0 mg) and the resulting suspension was stirred under hydrogen atmosphere for 2 h. The mixture was filtered through a syringe filter into 0.3% aqueous trifluoroacetic acid (TFA) (50 ml), and the formed solution was frozen and lyophilized. The crude TFA salt was purified by preparative HPLC (0.1% TFA in water + 3% acetonitrile to 10% acetonitrile in 10 min, 12 ml min⁻¹ flow rate, peak eluted at 5.0 min) to give c-Epi ((5*R,6R*)-6-(methylamino)-5,6,7,8-tetrahydronaphthalene-1,2,5-triol trifluoroacetate) as a white powder (142 mg, 74% yield).

Preparation of the β₂AR–G_s complex for cryo-EM imaging

The β₂AR–G_s complex was prepared essentially in the same way as described previously² using the agonist c-Epi. Briefly, the receptor was incubated with the agonist c-Epi for 1 h at room temperature before the addition of a 1.2-fold molar excess of purified G protein. The coupling reaction was allowed to proceed at room temperature for 90 min and was followed by the addition of apyrase to generate a stable nucleotide-free complex. After 90 min incubation at room temperature, the complex was diluted in a buffer containing 20 mM HEPES pH 7.5, 100 mM NaCl, 10 µM c-Epi, 1% lauryl maltose neopentyl glycol (LMNG) and 0.1% CHS to initiate detergent exchange. Afterwards, the complex was purified by M1 FLAG affinity chromatography

to remove excess G protein and residual DDM. The M1 FLAG resin was first washed with buffer containing 1% LMNG, followed by washes with decreasing LMNG concentrations. After elution of the complex with 20 mM HEPES pH 7.5, 100 mM NaCl, 0.01% LMNG, 0.001% CHS, 5 mM EDTA, 0.2 mg ml⁻¹ FLAG peptide and 10 µM c-Epi, the protein was supplemented with 100 µM TCEP and stored overnight at 4 °C. The complex was further purified by size-exclusion chromatography on a Superdex200 Increase 10/300GL (Cytiva) in 20 mM HEPES pH 7.5, 100 mM NaCl, 100 µM TCEP, 0.001% LMNG, 0.0001% CHS and 10 µM c-Epi. With the addition of 2 mM MgCl₂ in the buffer of complex used for GTP experiments. Monodisperse fractions were concentrated with a 100 kDa MWCO Amicon filter.

Cryo-EM grid preparation

The nucleotide-free β₂AR–G_s^{EMPTY} complex sample, 15 mg ml⁻¹, supplemented with 0.05% octyl-β-D-glucopyranoside was applied to glow-discharged holey carbongrids (Quantifoil R1.2/1.3). The grids were blotted for 2 s using an FEI Vitrobot Mark IV (ThermoFisher) at 20 °C and 100% humidity and then plunge frozen in liquid ethane. For the β₂AR–G_s^{GTP} complex samples, 16 mg ml⁻¹, supplemented with 0.02% octyl-β-D-glucopyranoside was applied to glow-discharged UltrAuFoil holey gold grids (Quantifoil, Au300-R1.2/1.3). GTP was added to the grid at a final concentration of 1 mM and the grids were blotted using an FEI Vitrobot Mark IV (ThermoFisher) at 4 °C and 100% humidity and then plunge frozen in liquid ethane at set time points post addition of GTP, adjusted by changing the total of blot time and wait time on the Vitrobot settings (2, 7 and 14 s). By measuring the time to freeze between the addition of GTP and ethane immersion using a stopwatch, we found that Vitrobot settings of 2, 7 and 14 seconds equated to 5, 10 and 17 seconds, respectively, in actual time (Extended Data Fig. 2a).

Cryo-EM data collection

Cryo-EM imaging of the nucleotide-free β₂AR–G_s^{EMPTY} complex was performed on a Titan Krios (ThermoFisher) electron microscope equipped with a K2 Summit direct electron detector (Gatan) and post-column energy filter. The microscope was operated at 300 kV accelerating voltage, with a nominal magnification of ×130,000 in counting mode resulting in a magnified pixel size of 1.06 Å. Videos were obtained at an exposure of 1.3 electrons per Å² per frame with 40 frames per video stack and defocus ranging from -1.2 to -2.5 µm. Automatic data acquisition was performed using SerialEM (v.3.6 and v.3.9)⁶⁴ for all datasets. Cryo-EM imaging of the β₂AR–G_s^{GTP (5sec)} complex was performed on a Titan Krios (ThermoFisher) electron microscope equipped with a K3 Summit direct electron detector (Gatan). The microscope was operated at 300 kV accelerating voltage, with a nominal magnification of ×105,000 in super-resolution mode resulting in a magnified pixel size of 0.43385 Å. Videos were obtained at a total exposure of 60.48 electrons per Å² over 63 frames with defocus ranging from -1.0 to -2.0 µm. Cryo-EM imaging of β₂AR–G_s^{GTP (10sec)} complex utilized a Titan Krios (ThermoFisher) electron microscope equipped with a K3 Summit direct electron detector (Gatan). The microscope was operated at 300 kV accelerating voltage, with a magnification at camera of ×58,679 in super-resolution mode resulting in a magnified pixel size of 0.42605 Å. For the first and second grid, videos were obtained at an exposure rate of 21.13 electrons per Å² per second with defocus ranging from -0.4 to -2.0 µm. The total exposure time was 2.717 s over 77 frames per video stack. For an additional collection of the first grid, videos were obtained at an exposure rate of 20.95 electrons per Å² per second with defocus ranging from -0.4 to -2.0 µm. The total exposure time was 2.717 s over 77 frames per video stack. For a third grid, videos were obtained at an exposure rate of 30.71 electrons Å² second with defocus ranging from -0.5 to -1.6 µm. The total exposure time was 2.008 s over 79 frames per video stack. Cryo-EM imaging of β₂AR–G_s^{GTP (17sec)} was performed on a Titan Krios (ThermoFisher) electron microscope operated at 300 kV accelerating voltage, and equipped with a K3 Summit direct electron

detector (Gatan) and post-column energy filter, with a magnification of $\times 105,000$ in super-resolution mode resulting in a magnified pixel size of 0.43385 \AA . Videos were obtained at an exposure rate of 32.46 electrons per \AA^2 per s with defocus ranging from -0.4 to -0.9 \mu m . The total exposure time was 1.999 s over 79 frames per video stack.

Image processing and 3D reconstruction

Preprocessing of all datasets was carried out similarly, and all processing was performed using cryoSPARC⁶⁵. Dose-fractionated image stacks were subjected to beam-induced motion correction and dose-weighting using patch motion correction. For datasets collected at super-resolution, the videos were binned by 2 during motion correction. Contrast transfer function (CTF) parameters for each non-dose-weighted micrograph were determined by patch CTF followed by curation of micrographs for quality. For the $\beta_2\text{AR}-\text{G}_s^{\text{EMPTY}}$ complex, $4,190,258$ particles from $7,176$ micrographs were extracted using semi-automated particle selection. Subsequently, two rounds of 2D classification and three rounds of 3D classification (coupled ab initio and heterogeneous refinement operations) were performed on a binned dataset (pixel size 4.24 \AA and 2.12 \AA , respectively). A refined set of $375,915$ unbinned particles (1.06 \AA per pixel) was subjected to homogeneous and local refinement. CryoSPARC 3DVA²⁹ was used to determine conformational heterogeneity in the final dataset. The former set of particles was processed by 3DVA with three modes, and a mask encompassing the AHD flexible region. Following 3DVA, the first principal component (PCO) was subjected to intermediate 3DVA display processing with a window of 2 , which sorted particles into 20 overlapping classes that were subsequently processed by local refinement to mask out the detergent micelle.

For the $\beta_2\text{AR}-\text{G}_s^{\text{GTP}(\text{5sec})}$ complex, $5,006,746$ particles from $6,010$ micrographs were extracted using semi-automated particle selection. Subsequently, two rounds of 2D classification and six rounds of 3D classification (coupled ab initio and heterogeneous refinement operations) were performed on a binned dataset (pixel size 3.471 \AA and 1.7354 \AA , respectively). A refined set of $329,376$ unbinned particles (0.8677 \AA per pixel) was subjected to homogeneous and local refinement. 3DVA was used to determine conformational heterogeneity in the final dataset. The former set of particles was processed by 3DVA with three modes, and a mask encompassing the AHD flexible region. Following 3DVA, the first principal component (PCO) was subjected to intermediate 3DVA display processing with a window of 2 , which sorted particles into 20 overlapping classes that were subsequently processed by local refinement to mask out the detergent micelle. For the $\beta_2\text{AR}-\text{G}_s^{\text{GTP}(\text{10sec})}$ complex, a total of $9,706,318$ particles from $16,360$ micrographs across the collection of four separate grids were extracted using semi-automated particle selection. Subsequently, the particles from each collection were separately subjected to 5 – 7 rounds of 2D classification and 1 – 5 rounds of 3D classification (coupled ab initio and heterogeneous refinement operations) performed on binned datasets (pixel size 3.408 \AA and 1.7042 \AA , respectively). The particles were then merged to create a refined set of $689,807$ unbinned particles (0.8521 \AA per pixel), which were subjected to an additional two rounds of 3D classification (ab initio coupled with heterogeneous refinement), then homogeneously refined. 3DVA was then used to determine conformational heterogeneity in the final dataset. The former set of particles was processed by 3DVA with three modes, and a mask encompassing the AHD flexible region. Following 3DVA, the first principal component (PCO) was subjected to intermediate 3DVA display processing with a window of 2 , which sorted particles into 20 overlapping classes that were subsequently processed by local refinement to mask out the detergent micelle. For the $\beta_2\text{AR}-\text{G}_s^{\text{GTP}(\text{17sec})}$ complex, $5,252,019$ particles from $10,010$ micrographs were extracted using semi-automated particle selection. Subsequently, eight rounds of 2D classification and four rounds of 3D classification (coupled ab initio and heterogeneous refinement operations) were performed on a binned dataset (pixel size

3.471 \AA and 1.735 \AA , respectively). A refined set of $213,033$ unbinned particles (0.8677 \AA per pixel) was subjected to homogeneous and local refinement. 3DVA was used to determine conformational heterogeneity in the final dataset. The set of particles was processed by 3DVA with three modes, and a mask encompassing the AHD flexible region. Following 3DVA, the first principal component (PCO) was subjected to intermediate 3DVA display processing with a window of 2 , which sorted particles into 20 overlapping classes that were subsequently processed by local refinement to mask out the detergent micelle. The $\beta_2\text{AR}-\text{G}_s^{\text{GTP}(\text{Merge})}$ dataset consisted of the refined particle sets of the $\beta_2\text{AR}-\text{G}_s^{\text{GTP}(\text{5sec})}$, $\beta_2\text{AR}-\text{G}_s^{\text{GTP}(\text{10sec})}$ and $\beta_2\text{AR}-\text{G}_s^{\text{GTP}(\text{17sec})}$ complex datasets that were re-extracted and the particles from the $\beta_2\text{AR}-\text{G}_s^{\text{GTP}(\text{10sec})}$ dataset were Fourier cropped to obtain an equivalent pixel size (0.8677 \AA per pixel). The particles were then homogeneously refined together before either a final round of 3D classification or processing by 3DVA. The 3D classification into 20 classes was performed without alignment and using a mask on the $\text{G}\alpha$ subunit (RLD and AHD flexible region). Following 3D classification, the particles of each class were locally refined to generate reconstructions with the micelle masked out. 3DVA was run with three modes, and a mask encompassing the AHD flexible region. Following 3DVA, the first principal component (PCO) was subjected to intermediate 3DVA display processing with a window of $0, 1$ or 2 , which sorted particles into 20 discrete (window of 0) or overlapping (windowing of 1 or 2) classes that were subsequently processed by local refinement to mask out the detergent micelle. The resulting 20 particle sets were additionally locally refined with a mask encompassing the receptor only. UCSF Chimera (v.1.16)⁶⁶, UCSF ChimeraX (v.1.6 and v.1.7)⁶⁷ and Protein Imager⁶⁸ were used for map/model visualization. 3DFSC was used to calculate Fourier shell correlation curves, directional orientation, power spectra and sphericity scores presented in Supplementary Fig. 1 and Supplementary Table 2.

Molecular modelling

The X-ray crystal structure of $\beta_2\text{AR}-\text{G}\alpha_s$ (PDB 3SN6)² was used as the initial model for the complex in the open AHD conformation, whereas a composite of PDB 3SN6 with the $\text{G}\alpha_s$ -GTPyS crystal structure (PDB 1AZT)⁴⁵ was used to generate an initial model for closed reconstructions. The initial models were placed into respective cryo-EM maps using the Chimera ‘fit-in-map’ function. To improve the modelling, iterative rounds of interactive model adjustment in Coot (v.0.9.8.1EL)⁶⁹, followed by real-space refinement in Phenix (v.1.20.1-4487)⁷⁰ using secondary structure restraints in addition to the default restraints, were completed. Once confidence in the side chain placement of $\beta_2\text{AR}$ was reached for the ligand-binding pocket, the GemSpot pipeline⁷¹ utility of Maestro v.13.8 (Schrödinger) was used to dock c-Epi into the maps. Then, iterative modelling continued and the final models generated using Phenix refinement. To generate preliminary models for MD simulations the refined models from the global reconstructions (including receptor and G protein) were amended with the local receptor models generated from local refinement of the receptor alone, and then missing architecture (for example, AHD) was further built out into low-resolution density using the unsharpened global map to achieve as close an approximation to experimental data as possible. These preliminary models were then further prepared for MD simulations as described below.

Cryo-EM map and model analysis

To determine the angle of $\text{G}\alpha_s$ AHD opening, models with open and closed AHD were aligned to the Ras domain in ChimeraX⁶⁷. Angle of opening is defined as the angle between the centre of mass of the closed AHD (residues 88–202), the RHD (residues 203–394) and the open AHD (residues 88–202). The movement of GTP within the nucleotide-binding pocket over the 3DVA intermediates was determined by measuring the average change in distance between the nucleotide purine ring and phosphate atoms of the GTP molecule after structures were aligned to

Article

the G_s RHD. To measure comparative volume of density in the open versus the closed conformation (Extended Data Fig. 2) the AHD was docked into frames 1 (maximally open AHD) and 20 (maximally closed) of each 3DVA trajectory, then a region of 6 Å from the docked AHD structures was used to define ‘fully open’ or ‘fully closed’, respectively. The volume of reconstruction EM density, at a threshold volume level 0.05, that was encompassed in the defined regions was calculated using ChimeraX⁶⁷. Further model analysis (Extended Data Fig. 8l,m and Supplementary Table 4) was carried out using Python Jupyter Notebooks⁷² scripted using the Python modules mdciao⁷³.

Negative-stain EM

The β₂AR–G_s was visualized by negative-stain EM either alone (nucleotide-free) or post addition of GTP at time points of 20 s, 40 s or 10 min. All samples were prepared with a conventional negative-staining protocol⁷⁴, with 10 s incubation on 300 mesh carbon–copper support grids (EMS). Images were collected using a Morgagni 100 kV transmission electron microscope equipped with an Orius camera (Gatan), at a pixel size of 1.623 Å. Micrographs were processed in cryoSPARC to obtain 2D particle averages. For the complex-alone dataset, 24,579 particles were initially picked from 111 micrographs; for the 20 seconds. For the GTP dataset, 15,428 particles were initially picked from 94 micrographs; for the 40 seconds. For the GTP dataset 12,440 particles were initially picked from 105 micrographs; for 10 min. The GTP dataset 16,621 particles were initially picked from 85 micrographs. The datasets were then curated using iterative rounds of 2D classification to generate final counts of 11,694 particles, 6,209 particles, 5,215 particles and 7,072 particles, for the 0, 20 s, 40 s and 10 min time-point datasets, respectively.

Molecular dynamics simulations

The β₂AR–G_s^{GTP(Merged)} initial structures were extracted from five intermediate frames (16–20). In the β₂AR the C terminus of TM5 and the N terminus of TM6 were capped at Arg239 and His269, respectively. In G_s^{GTP}, Cys2, Ser2, Ala2 and Leu394, Asn341, Cys68 were capped at the N and C termini in G_s, Gβ and Gγ subunits, respectively. The CHARMM-GUI builder⁷⁵ was used to model and embed the receptor into a pure 1-palmitoyl-2-oleyl-sn-glycero-3-phosphocholine bilayer of approximately 150 Å × 150 Å. The palmitoyl group was added to β₂AR at C341 and N-palmitoyl was added to G_s at Gly2, S-palmitoyl to G_s at Cys3 and S-geranylgeranyl to Gγ at Cys68. In both β₂AR and G_s^{GTP}, all residues were kept in their standard protonation states on the basis of their pK_a at pH 7, with the exception of Glu122, Asp130 and Asp79 in β₂AR, which were protonated to be consistent with previously published data⁷⁶. In the β₂AR, the C terminus of TM5 was capped at Arg239 by methylation and the N terminus of TM6 at His264 was capped by acetylation, respectively. We used standard N and C terminus patches for the rest of the G protein and the receptor. Each system was solvated in a rectangular box of 150 Å side length for X and Y and 120 Å for Z with TIP3P water⁷⁷ and a concentration of 0.10 M Na⁺/Cl⁻ ions. The CHARMM36 (ref. 78) force field was used for lipids, proteins and nucleotides. The CgenFF⁷⁹ generalized force field was implemented to describe the β₂AR ligand c-Epi. All five β₂AR–G_s^{GTP} intermediates were energy minimized with the steepest descents algorithm and 1,000 kJ mol⁻¹ nm⁻¹ as the threshold. All systems were equilibrated with harmonic positional restraints applied to lipids and Cα atoms of the protein that were sequentially released in a series of equilibration steps. All non-biased simulations were performed using the GROMACS (2022 simulation package)⁸⁰. The software VMD v.1.9 (ref. 81), NLG⁸², MDsr⁸³ and our own Python-based analysis package (mdcioao)⁷³ were used to visualize and analyse MD simulations. NPT simulations were performed at 310 K and 1 bar using the velocity rescaling⁸⁴ thermostat and Parrinello–Rahman barostat⁸⁵ with a 2 fs integration time step. The van der Waals interactions were gradually shifted to zero in the range between 10 and 12 Å. Long-range electrostatic interactions more than the cut-off 12 Å were calculated

using PME⁸⁶. Relevant hydrogen bond lengths were constrained using the LINCS algorithm⁸⁷. For all five intermediate frames (16–20), three independent 3 μs long NPT production runs were carried out for each system setup, starting with different initial velocities.

Analysis of molecular dynamics trajectories

Analysis of the MD simulation data was carried out using Python Jupyter Notebooks⁷² scripted using the Python modules mdciao⁷³ and MDtraj⁸⁸ for analysis of molecular simulation data. For cluster analysis of c-Epi, all MD trajectory data (Supplementary Table 6) was first aligned on the β₂AR of PDB 3SN6, such that the c-Epi ligand coordinates are relative to the same β₂AR scaffold. Then, principal component analysis^{89,90}, as implemented in PyEMMA⁹¹, was used on the Cartesian coordinates of all c-Epi atoms, yielding a common principal component (PC) space in which global c-Epi motion can be mapped, as shown in Extended Data Fig. 10i for the first two PCs, which already capture 65% of the total variance. Next, the density peak algorithm (DPA), as implemented by d’Errico et al.⁹² was used to cluster the data. DPA (Z = 1.75) using the first four PCs (greater than 80% variance) finds a total of 15 clusters/poses (Supplementary Table 6), of which 7 are shown in Extended Data Fig. 10 via their most representative pose. Using the assignment of the individual frames of each trajectory to either one of these 15 clusters, we can produce individual discrete trajectories for all MD datasets, showing how the system transitions between the c-Epi poses in Extended Data Fig. 10h.

Reporting summary

Further information on research design is available in the Nature Portfolio Reporting Summary linked to this article.

Data availability

The atomic coordinates of β₂AR–G_s^{EMPTY} (frames 1–20) have been deposited in the Protein Data Bank (PDB) under accession codes 8GDZ, 8GE1, 8GE2, 8GE3, 8GE4, 8GE5, 8GE6, 8GE7, 8GE8, 8GE9, 8GEA, 8GEB, 8GEC, 8GED, 8GEE, 8GEF, 8GEG, 8GEH, 8GEI and 8GEJ, respectively. The atomic coordinates of β₂AR–G_s^{GTP(Merged)} (Frames 1–20) have been deposited in the PDB under accession codes 8GFV, 8GFW, 8GFX, 8GFY, 8GFZ, 8GG0, 8GG1, 8GG2, 8GG3, 8GG4, 8GG5, 8GG6, 8GG7, 8GG8, 8GG9, 8GGA, 8GGB, 8GGC, 8GGE and 8GGF, respectively; along with the coordinates from corresponding localized maps of β₂AR under accession codes 8GGI, 8GGJ, 8GGK, 8GGL, 8GGM, 8GGN, 8GGO, 8GGP, 8GGQ, 8GGR, 8GGS, 8GGT, 8GGU, 8GGV, 8GGW, 8GGX, 8GGY, 8GGZ, 8GH0 and 8GH1, respectively. The atomic coordinates of β₂AR–G_s^{GTP(Merged)} (classes A–T) have been deposited in the PDB under accession codes 8UNL, 8UNM, 8UNN, 8UNO, 8UNP, 8UNQ, 8UNR, 8UNS, 8UNT, 8UNU, 8UNV, 8UNW, 8UNX, 8UNY, 8UNZ, 8UO0, 8UO1, 8UO2, 8UO3 and 8UO4, respectively. Cryo-EM maps of β₂AR–G_s^{EMPTY} (frames 1–20) have been deposited in the Electron Microscopy Data Bank (EMDB) under accession codes EMD-29951, EMD-29952, EMD-29953, EMD-29954, EMD-29955, EMD-29956, EMD-29958, EMD-29959, EMD-29960, EMD-29961, EMD-29962, EMD-29964, EMD-29965, EMD-29966, EMD-29967, EMD-29968, EMD-29969, EMD-29970, EMD-29971 and EMD-29972, respectively. Cryo-EM maps of β₂AR–G_s^{GTP(sec)} (frames 1–20) have been deposited in the EMDB under accession codes EMD-40096, EMD-40097, EMD-40098, EMD-40099, EMD-40100, EMD-40101, EMD-40102, EMD-40103, EMD-40104, EMD-40105, EMD-40106, EMD-40107, EMD-40108, EMD-40109, EMD-40110, EMD-40111, EMD-40112, EMD-40113, EMD-40114 and EMD-40115, respectively. Cryo-EM maps of β₂AR–G_s^{GTP(10sec)} (frames 1–20) have been deposited in the EMDB under accession codes EMD-40116, EMD-40117, EMD-40118, EMD-40119, EMD-40120, EMD-40121, EMD-40122, EMD-40123, EMD-40124, EMD-40125, EMD-40126, EMD-40127, EMD-40128, EMD-40129, EMD-40130, EMD-40131, EMD-40132, EMD-40133, EMD-40134 and EMD-40135, respectively. Cryo-EM maps of β₂AR–G_s^{GTP(17sec)} (frames 1–20) have been deposited in the EMDB under accession codes

- EMD-40136, EMD-40137, EMD-40138, EMD-40139, EMD-40140, EMD-40141, EMD-40142, EMD-40143, EMD-40144, EMD-40145, EMD-40146, EMD-40147, EMD-40148, EMD-40149, EMD-40150, EMD-40151, EMD-40152, EMD-40153, EMD-40154 and EMD-40155, respectively. Cryo-EM maps of β_2 AR-G_s^{GTP(Merged)} (frames 1–20) have been deposited in the EMDB under accession codes EMD-29985, EMD-29986, EMD-29987, EMD-29988, EMD-29989, EMD-29990, EMD-29991, EMD-29992, EMD-29993, EMD-29994, EMD-29995, EMD-29996, EMD-29997, EMD-29998, EMD-29999, EMD-40000, EMD-40001, EMD-40002, EMD-40004 and EMD-40005, respectively, along with the corresponding localized maps of β_2 AR under accession codes EMD-40009, EMD-40010, EMD-40011, EMD-40012, EMD-40013, EMD-40014, EMD-40015, EMD-40016, EMD-40017, EMD-40018, EMD-40019, EMD-40020, EMD-40021, EMD-40022, EMD-40023, EMD-40024, EMD-40025, EMD-40026, EMD-40027 and EMD-40028, respectively; and localized G-protein maps under accession codes EMD-40156, EMD-40157, EMD-40158, EMD-40159, EMD-40160, EMD-40161, EMD-40163, EMD-40164, EMD-40165, EMD-40166, EMD-40167, EMD-40168, EMD-40169, EMD-40170, EMD-40171, EMD-40172, EMD-40173, EMD-40174, EMD-40175 and EMD-40176, respectively. Cryo-EM maps of β_2 AR-G_s^{GTP(Merged)} (classes A–T) have been deposited in the EMDB under accession codes EMD-42408, EMD-42409, EMD-42410, EMD-42411, EMD-42412, EMD-42413, EMD-42414, EMD-42415, EMD-42416, EMD-42417, EMD-42418, EMD-42419, EMD-42420, EMD-42421, EMD-42422, EMD-42423, EMD-42424, EMD-42425, EMD-42426 and EMD-42427, respectively. Raw cryo-EM image data have been deposited in the Electron Microscopy Public Image Archive (EMPIAR) under ascension codes EMPIAR-11855, EMPIAR-11856, EMPIAR-11857 and EMPIAR-11858 for the β_2 AR-G_s^{EMPTY}, β_2 AR-G_s^{GTP(5sec)}, β_2 AR-G_s^{GTP(10sec)} and β_2 AR-G_s^{GTP(17sec)} datasets, respectively. Visualizations of MD trajectories are made available via MDsrv sessions included in a Zenodo dataset associated with this manuscript (<https://doi.org/10.5281/zenodo.1054878>)⁹³. Coordinates of comparison structures were available and obtained through the Protein Data Bank, under accession codes: 3SN6 (ref. 2), 1AZT (ref. 45), 2RH1 (ref. 47), 7LOQ (ref. 30) and 7RKF (ref. 50).
63. Hilger, D. et al. Structural insights into differences in G protein activation by family A and family B GPCRs. *Science* <https://doi.org/10.1126/science.aba3373> (2020).
64. Mastronarde, D. N. Automated electron microscope tomography using robust prediction of specimen movements. *J. Struct. Biol.* **152**, 36–51 (2005).
65. Punjani, A., Rubinstein, J. L., Fleet, D. J. & Brubaker, M. A. cryoSPARC: algorithms for rapid unsupervised cryo-EM structure determination. *Nat. Methods* **14**, 290–296 (2017).
66. Pettersen, E. F. et al. UCSF Chimera—a visualization system for exploratory research and analysis. *J. Comput. Chem.* **25**, 1605–1612 (2004).
67. Pettersen, E. F. et al. UCSF ChimeraX: structure visualization for researchers, educators, and developers. *Protein Sci.* **30**, 70–82 (2021).
68. Tomasello, G., Armenia, I. & Molla, G. The Protein Imager: a full-featured online molecular viewer interface with server-side HQ-rendering capabilities. *Bioinformatics* **36**, 2909–2911 (2020).
69. Emsley, P., Lohkamp, B., Scott, W. G. & Cowtan, K. Features and development of Coot. *Acta Crystallogr. D* **66**, 486–501 (2010).
70. Liebschner, D. et al. Macromolecular structure determination using X-rays, neutrons and electrons: recent developments in Phenix. *Acta Crystallogr. D* **75**, 861–877 (2019).
71. Robertson, M. J., van Zundert, G. C. P., Borrelli, K. & Skiniotis, G. GemSpot: a pipeline for robust modeling of ligands into Cryo-EM maps. *Structure* <https://doi.org/10.1016/j.str.2020.04.018> (2020).
72. Kluwyer, T. et al. Jupyter Notebooks - a publishing format for reproducible computational workflows. in *International Conference on Electronic Publishing* (eds Loizides, F. & Schmidt, B.) 87–90 (IOS Press, 2016).
73. Pérez-Hernández, G. & Hildebrand, P. W. mdciao: accessible analysis and visualization of molecular dynamics simulation data. Preprint at *bioRxiv* <https://doi.org/10.1101/2022.07.15.500163> (2022).
74. Peisley, A. & Skiniotis, G. 2D projection analysis of GPCR complexes by negative stain electron microscopy. *Methods Mol. Biol.* **1335**, 29–38 (2015).
75. Jo, S., Kim, T., Iyer, V. G. & Im, W. CHARMM-GUI: a web-based graphical user interface for CHARMM. *J. Comput. Chem.* **29**, 1859–1865 (2008).
76. Dror, R. O. et al. Identification of two distinct inactive conformations of the β_2 -adrenergic receptor reconciles structural and biochemical observations. *Proc. Natl Acad. Sci. USA* **106**, 4689–4694 (2009).
77. Jorgensen, W. L., Chandrasekhar, J., Madura, J. D., Impey, R. W. & Klein, M. L. Comparison of simple potential functions for simulating liquid water. *J. Chem. Phys.* **79**, 926–935 (1983).
78. Klauda, J. B. et al. Update of the CHARMM all-atom additive force field for lipids: validation on six lipid types. *J. Phys. Chem. B* **114**, 7830–7843 (2010).
79. Vanommeslaeghe, K. et al. CHARMM general force field: a force field for drug-like molecules compatible with the CHARMM all-atom additive biological force fields. *J. Comput. Chem.* **31**, 671–690 (2010).
80. Abraham, M. J. et al. GROMACS: high performance molecular simulations through multi-level parallelism from laptops to supercomputers. *SoftwareX* **1–2**, 19–25 (2015).
81. Humphrey, W., Dalke, A. & Schulten, K. VMD: visual molecular dynamics. *J. Mol. Graph.* **14**, 33–38 (1996). 27–38.
82. Rose, A. S. & Hildebrand, P. W. NGL Viewer: a web application for molecular visualization. *Nucleic Acids Res.* **43**, W576–W579 (2015).
83. Tiemann, J. K. S., Guijá-González, R., Hildebrand, P. W. & Rose, A. S. MDsrv: viewing and sharing molecular dynamics simulations on the web. *Nat. Methods* **14**, 1123–1124 (2017).
84. Bussi, G., Donadio, D. & Parrinello, M. Canonical sampling through velocity rescaling. *J. Chem. Phys.* **126**, 014101 (2007).
85. Parrinello, M. & Rahman, A. Polymorphic transitions in single crystals: a new molecular dynamics method. *J. Appl. Phys.* **52**, 7182–7190 (1981).
86. Darden, T., York, D. & Pedersen, L. Particle mesh Ewald: an $N\log(N)$ method for Ewald sums in large systems. *J. Chem. Phys.* **98**, 10089–10092 (1993).
87. Hess, B., Bekker, H., Berendsen, H. J. C. & Fraaije, J. G. E. M. LINCS: a linear constraint solver for molecular simulations. *J. Comput. Chem.* **18**, 1463–1472 (1997).
88. McGibbon, R. T. et al. MDTraj: a modern open library for the analysis of molecular dynamics trajectories. *Biophys. J.* **109**, 1528–1532 (2015).
89. Pearson, K. LIII. On lines and planes of closest fit to systems of points in space. *Lond. Edinb. Dublin Philos. Mag. J. Sci.* **2**, 559–572 (1901).
90. Hotelling, H. Analysis of a complex of statistical variables into principal components. *J. Educ. Psychol.* **24**, 417–441 (1933).
91. Scherer, M. K. et al. PyEMMA 2: A Software Package for Estimation, Validation, and Analysis of Markov Models. *J. Chem. Theory Comput.* **11**, 5525–5542 (2015).
92. d'Errico, M., Facco, E., Laio, A. & Rodriguez, A. Automatic topography of high-dimensional data sets by non-parametric density peak clustering. *Inf. Sci.* **560**, 476–492 (2021).
93. Pérez-Hernández, G., Batebi, H., & Hildebrand, P. W. Molecular simulation data associated with the manuscript 'Time-resolved cryo-EM of G protein activation by a GPCR'. Zenodo <https://doi.org/10.5281/zenodo.1054878> (2024).
94. Tan, Y. Z. et al. Addressing preferred specimen orientation in single-particle cryo-EM through tilting. *Nat. Methods* **14**, 793–796 (2017).

Acknowledgements Research reported in this publication was supported by equipment access through the Stanford Cryo-Electron Microscopy Center (cEMc). This work was funded by National Institutes of Health grants K99HL16140601 (to M.M.P.-S.), R01GM083118 (to G.S. and B.K.K.) and R01NS028471 (to B.K.K.) and Deutsche Forschungsgemeinschaft (DFG, German Research Foundation) DFG grants GRK 1910 and GM 13/14-1 (to P.G.) and SFB1423, project number 421152132, subproject C01, Stiftung Charité and the Einstein Center Digital for Future (to P.W.H.). We acknowledge the scientific support and HPC resources provided by the Erlangen National High Performance Computing Center (NHR@FAU) of the Friedrich-Alexander-Universität Erlangen-Nürnberg (FAU) under NHR project p10tae. NHR funding is provided by federal and Bavarian state authorities. NHR@FAU hardware is partially funded by the German Research Foundation (DFG)-440719683.

Author contributions M.M.P.-S. prepared cryo-EM grids, collected, analysed and processed cryo-EM data to generate final cryo-EM reconstructions, built and refined atomic models, collected and processed negative-stain EM data, analysed data, prepared figures and wrote the manuscript. G.P.-H. performed data analysis of cryo-EM models and MD simulations and contributed to figure development. H.B. performed MD simulations and data analysis and contributed to figure development. Y.G. prepared complex and prepared cryo-EM grids and generated a preliminary cryo-EM reconstruction for the 5s GTP time point. G.E. prepared cryo-EM grids, collected, analysed and generated preliminary reconstructions for the 3D-classified nucleotide-free states with the assistance of A.B.S. G.E. and D.H. optimized conditions to obtain stable complexes for the study. D.H. purified and prepared β_2 AR-G_s complexes. O.P. collected cryo-EM data for the 5s GTP time point. M.C. purified β_2 AR and G_s, and prepared β_2 AR-G_s complexes. F.H. purified G_s and assisted complex preparation. L.M. synthesized c-Epi. P.G. supervised the synthesis of c-Epi. B.K.K. oversaw protein purification and β_2 AR-G_s complexation. P.W.H. supervised molecular dynamics studies. G.S. oversaw cryo-EM studies and conceived and supervised the project. M.M.P.-S. and G.S. wrote the manuscript.

Competing interests G.S. is a co-founder of, and consultant for, Deep Apple Therapeutics. B.K.K. is a co-founder of, and consultant for, ConformatRx.

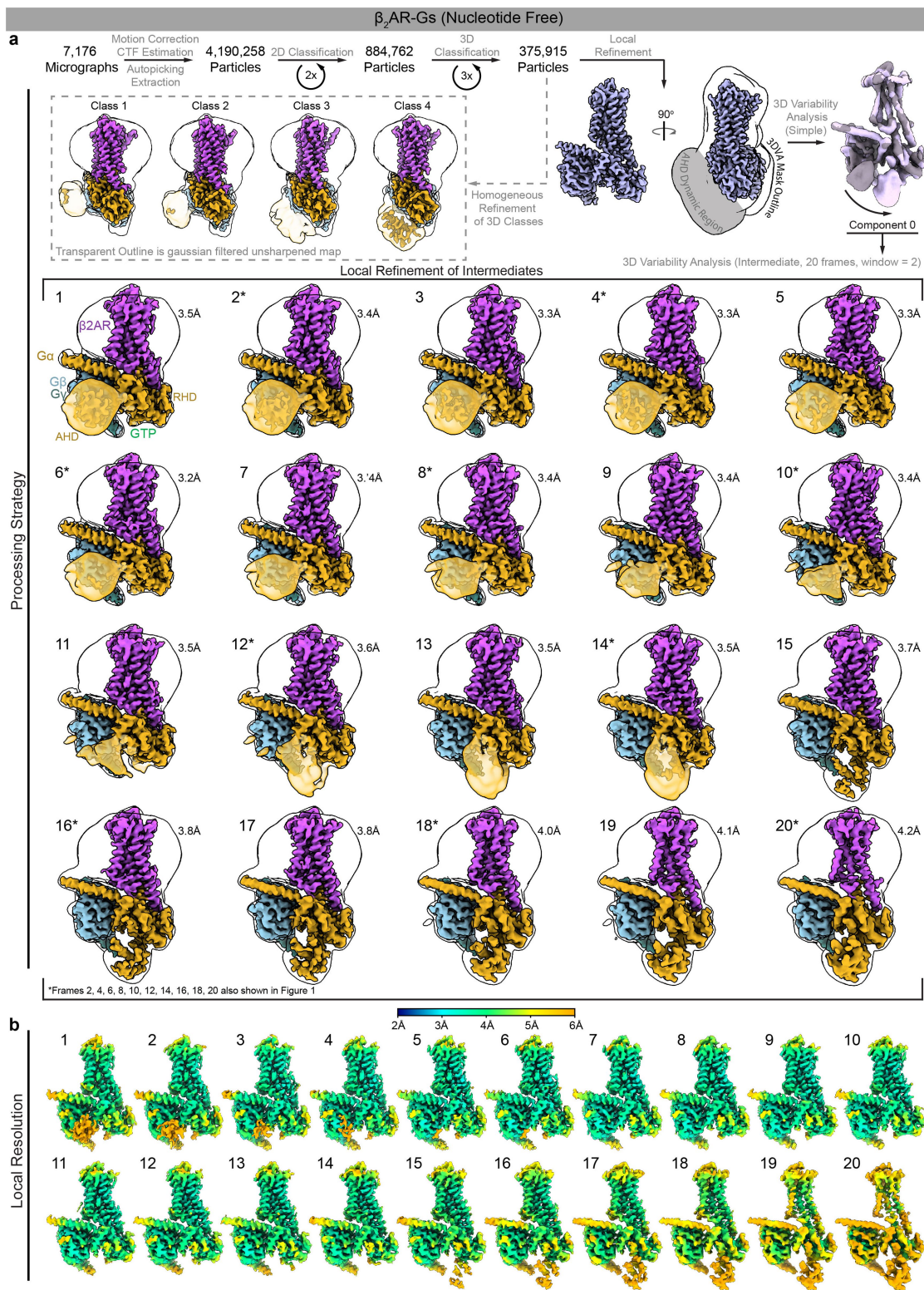
Additional information

Supplementary information The online version contains supplementary material available at <https://doi.org/10.1038/s41586-024-07153-1>.

Correspondence and requests for materials should be addressed to Georgios Skiniotis.

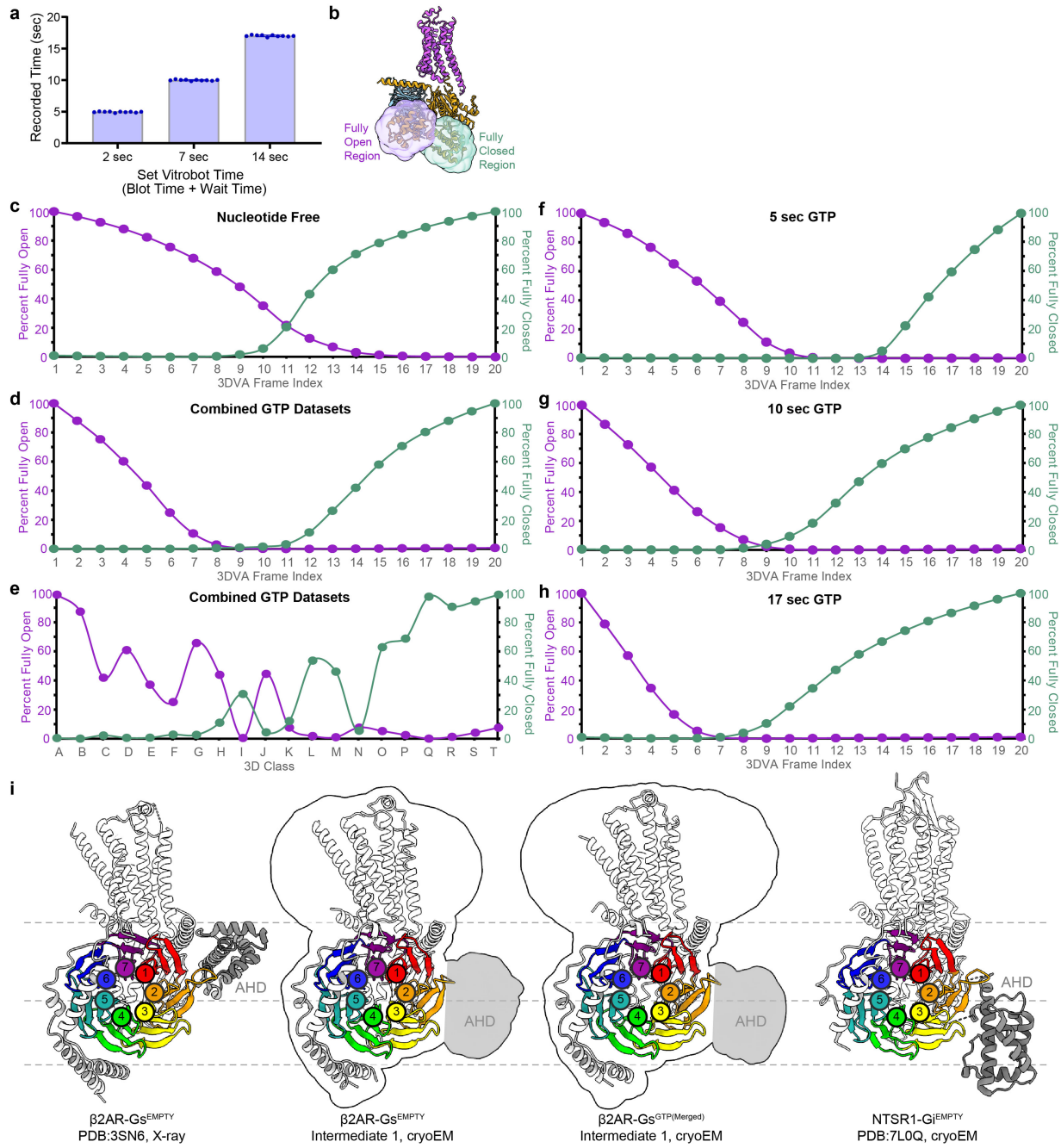
Peer review information *Nature* thanks the anonymous reviewers for their contribution to the peer review of this work. Peer reviewer reports are available.

Reprints and permissions information is available at <http://www.nature.com/reprints>.



Extended Data Fig. 1 | Cryo-EM processing and reconstruction of β_2 AR-Gs^{EMPTY}. **a**, Flow chart outlining the cryo-EM processing of β_2 AR-Gs^{EMPTY} complex using cryoSPARC^{29,65}. Local refinement reconstructions are shown with a Gaussian filtered map outline to show micelle and AHD densities. **b**, Local

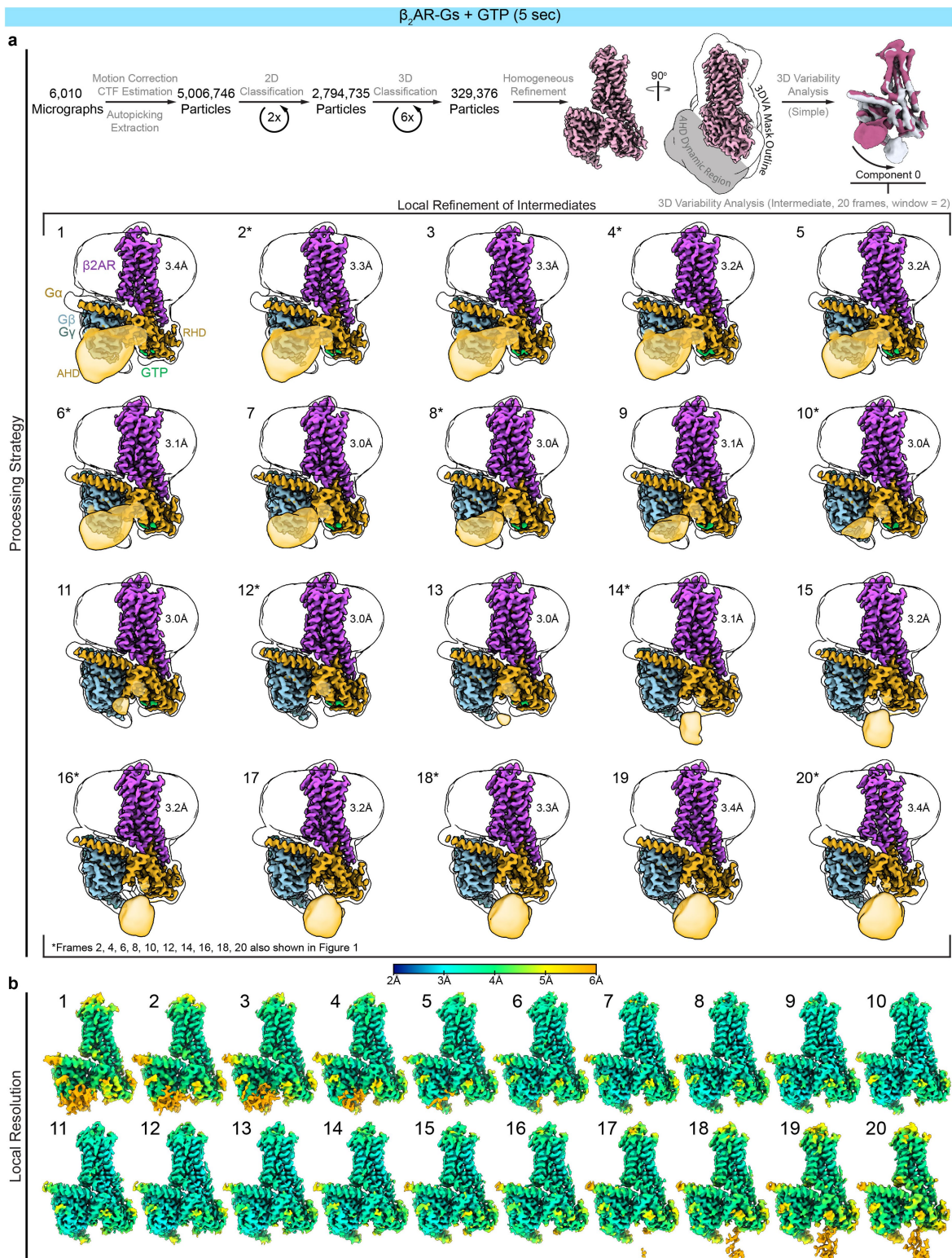
resolution of projections used in final cryo-EM reconstructions. See Supplementary Fig. 1 for associated 3DFSC⁹⁴ curves, directional orientation, power spectra, and angular distribution maps; and see Supplementary Table 2 for a table of sphericity scores.



Extended Data Fig. 2 | Dynamic residency of G α AHD in open and closed positions. **a**, Measurement of the real time of vitrification using a Vitrrobot. The Vitrrobot timing is the sum of user programmed blot time and wait time, 2 sec ($4.95 \text{ sec} \pm 0.026 \text{ S.E.M.}, n = 10$), 7 sec ($9.99 \text{ sec} \pm 0.029 \text{ S.E.M.}, n = 10$), 14 sec ($17.02 \text{ sec} \pm 0.040 \text{ S.E.M.}, n = 10$), where n indicates number of measurements recorded. Individual data points shown. **b-h**, To determine the residency of the AHD between open and closed positions in cryo-EM reconstructions, the AHD was docked into frames 1 (maximally open AHD) and 20 (maximally closed AHD) of each 3DVA trajectory (**c-d, f-h**) or 3D classes ordered from left, class A, to right, class T, by percent contribution of particles from the 17 sec dataset (**e**), a region of 6 Å from the docked structures was used to define ‘fully open’ or ‘fully closed’

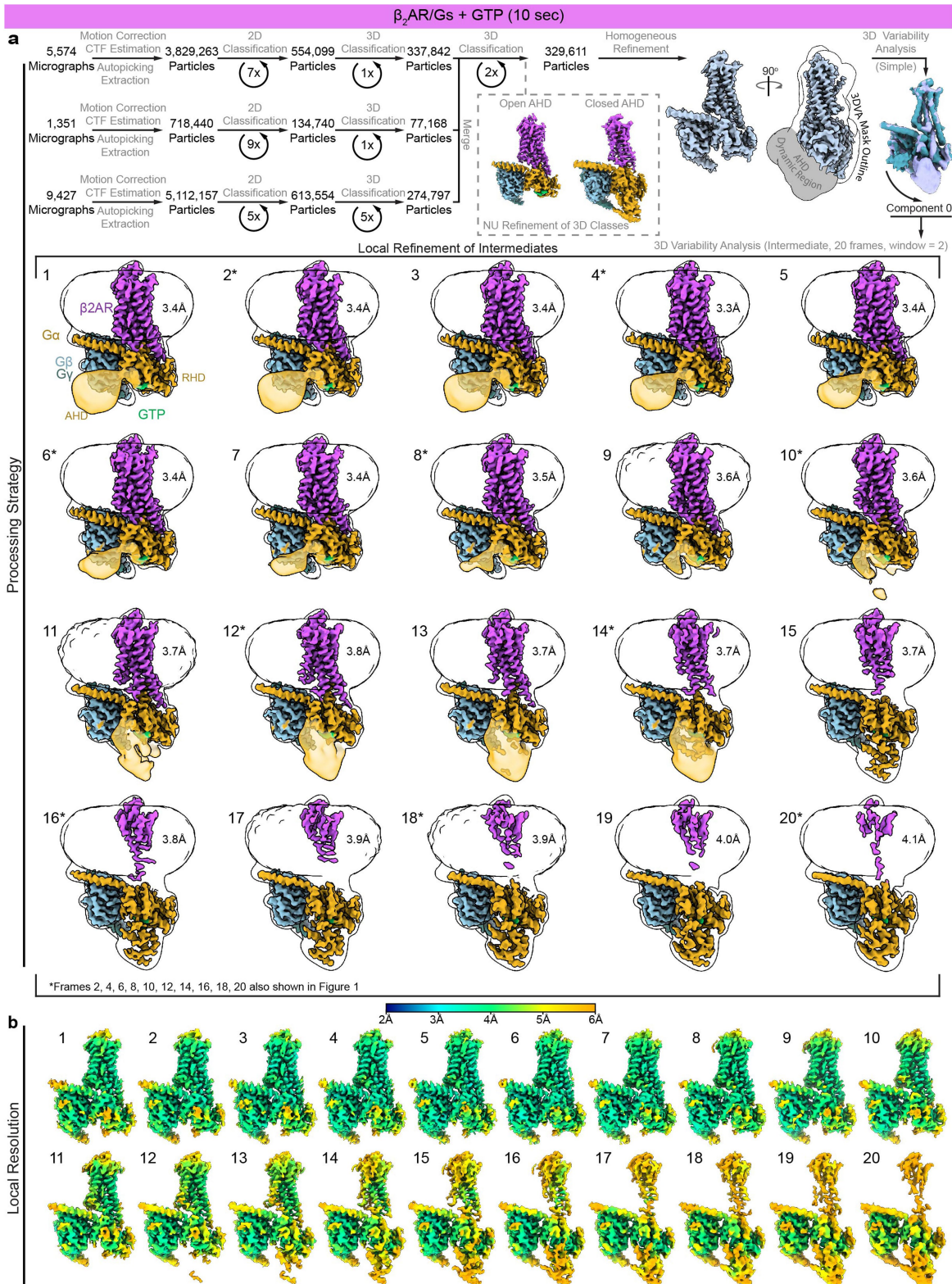
respectively, **b**, and the volume of cryo-EM map at a threshold level of 0.05 that was enclosed in the defined regions was determined. **c-g, i**, Location of G α AHD in relation to G β . The crystal structure (PDB:3SN6) locates the G α AHD (grey) adjacent to G β blades 1 (red) and 2 (orange) and interacting with blade 2. In contrast, the location of the cryo-EM density that corresponds to the AHD lies adjacent to G β blades 2 and 3 (yellow) in both the nucleotide-free and GTP conditions. The cryo-EM structure of NTSR1-Gi also has an open AHD adjacent to blades 2 and 3, but in a different orientation. Structures have been aligned to G β . In the middle panels, the cryo-EM density envelope (Gaussian filtered, $\sigma = 2$) of the unsharpened map is shown with the density corresponding to the location of the AHD shaded in grey.

Article



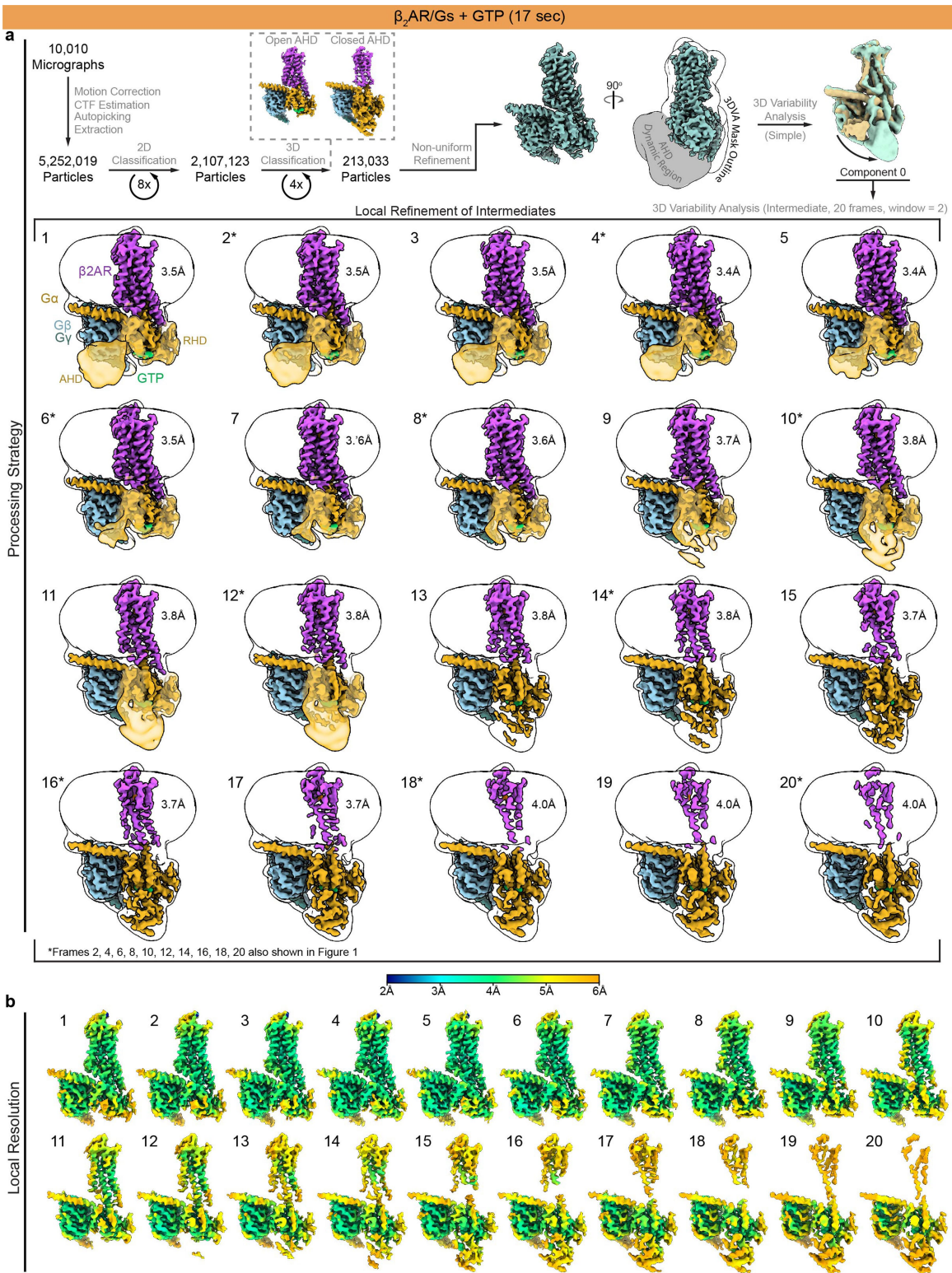
Extended Data Fig. 3 | Cryo-EM processing and reconstruction of $\beta_2\text{AR-Gs}^{\text{GTP}(5\text{sec})}$. **a**, Flow chart outlining the cryo-EM processing of $\beta_2\text{AR-Gs}^{\text{GTP}(5\text{sec})}$ complex using cryoSPARC^{29,65}. Local refinement reconstructions are shown with a Gaussian-filtered map outline to show micelle and AHD densities. **b**, Local

resolution of projections used in final cryo-EM reconstructions. See Supplementary Fig. 1 for associated 3DFSC⁹⁴ curves, directional orientation, power spectra, and angular distribution maps; and see Supplementary Table 2 for a table of sphericity scores.



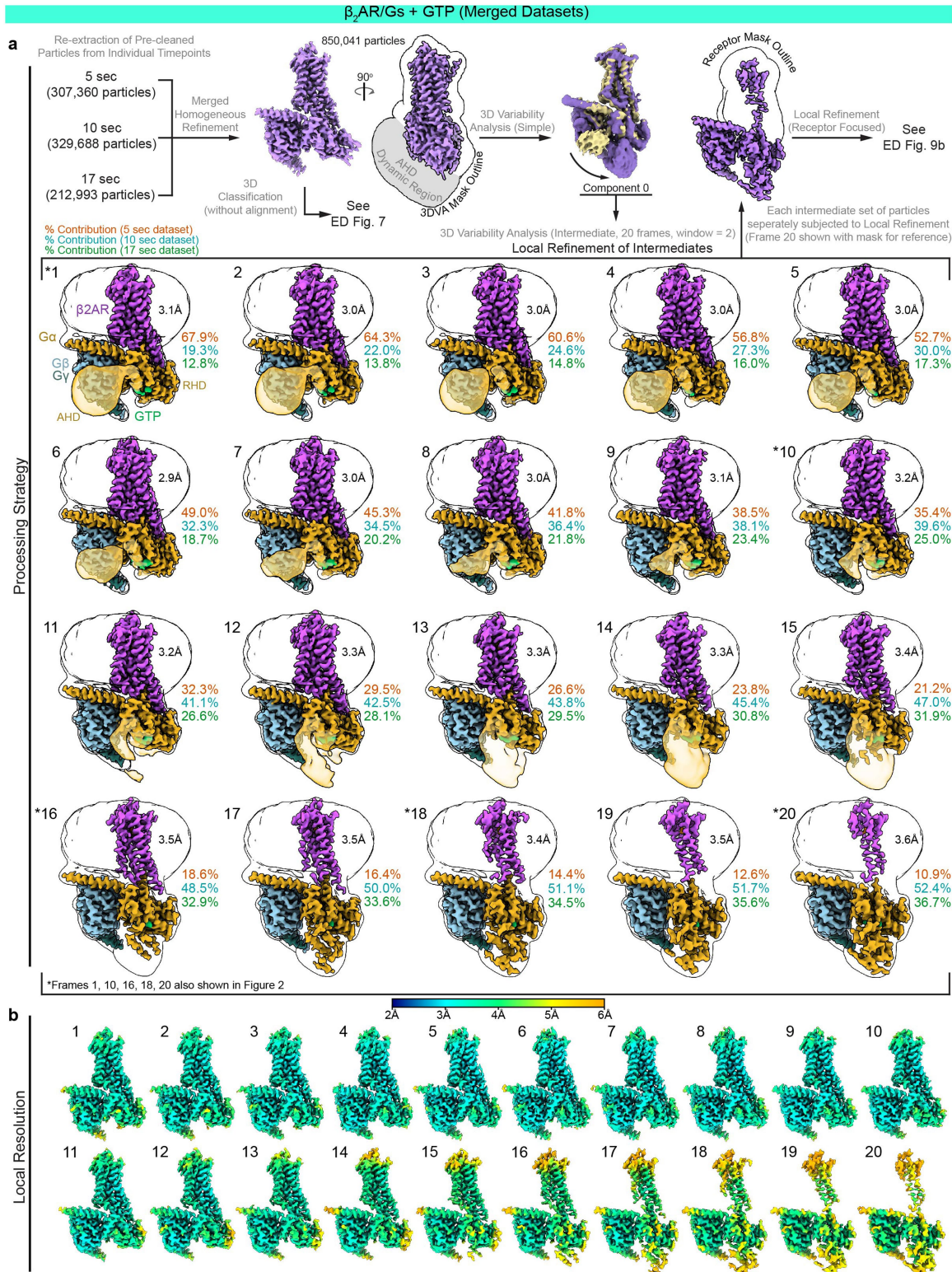
Extended Data Fig. 4 | Cryo-EM processing and reconstruction of β_2 AR-Gs^{GTP(10sec)}. **a**, Flow chart outlining the cryo-EM processing of β_2 AR-Gs^{GTP(10sec)} complex using cryoSPARC^{29,65}. Local refinement reconstructions are shown with a Gaussian filtered map outline to show micelle and AHD

densities. **b**, Local resolution of projections used in final cryo-EM reconstructions. See Supplementary Fig. 1 for associated 3DFSC⁹⁴ curves, directional orientation, power spectra, and angular distribution maps; and see Supplementary Table 2 for a table of sphericity scores.



Extended Data Fig. 5 | Cryo-EM processing and reconstruction of $\beta_2\text{AR-Gs}^{\text{GTP}(17\text{sec})}$. **a**, Flow chart outlining the cryo-EM processing of $\beta_2\text{AR-Gs}^{\text{GTP}(17\text{sec})}$ complex using cryoSPARC^{29,65}. Local refinement reconstructions are shown with a Gaussian filtered map outline to show micelle and AHD densities. **b**, Local

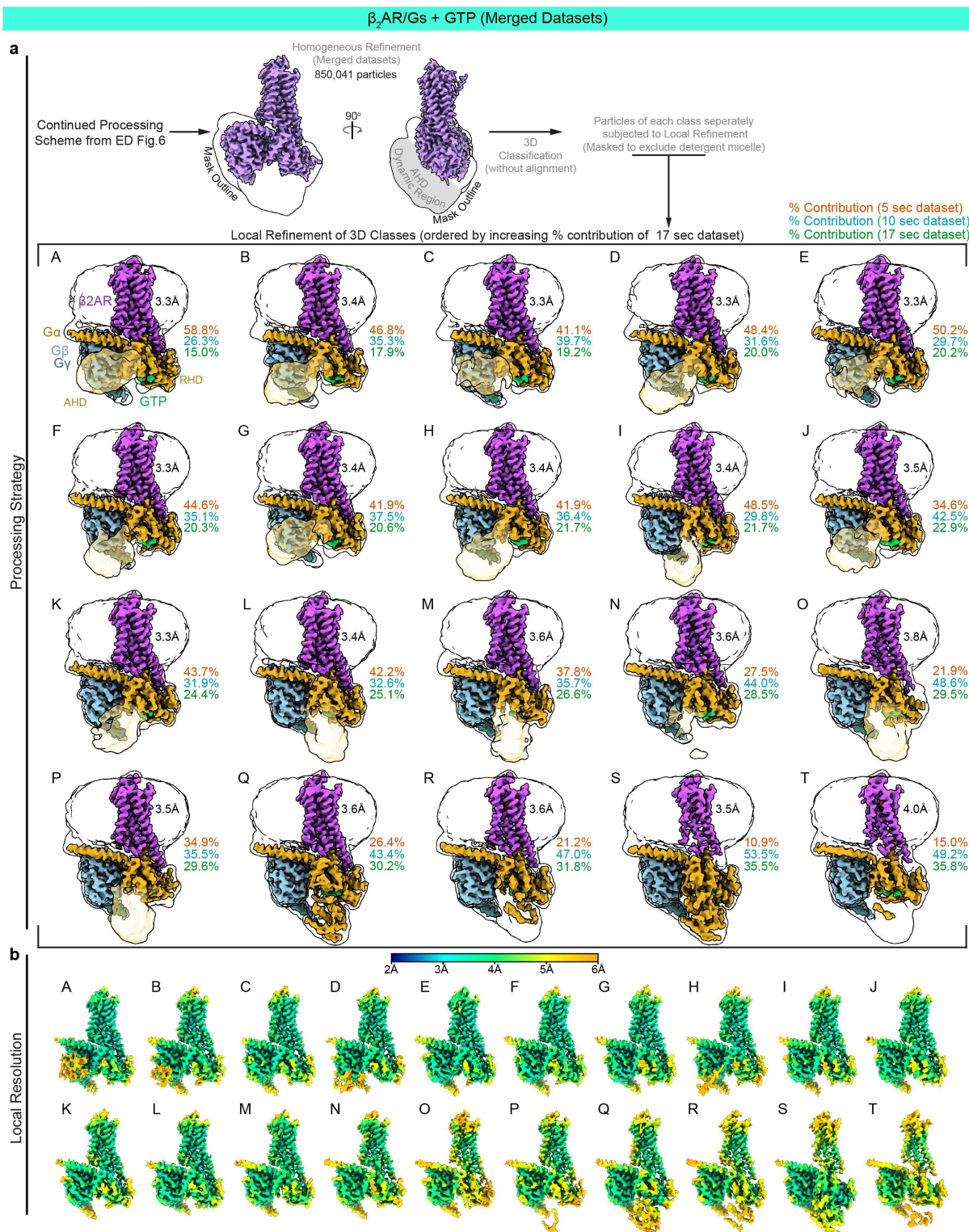
resolution of projections used in final cryo-EM reconstructions. See Supplementary Fig. 12 for associated 3DFSC⁹⁴ curves, directional orientation, power spectra, and angular distribution maps; and see Supplementary Table 2 for a table of sphericity scores.



Extended Data Fig. 6 | Cryo-EM processing and reconstruction of β_2 AR-Gs^{GTP(Merged)}. **a.**, Flow chart outlining the cryo-EM processing of β_2 AR-Gs^{GTP(Merged)} complex using cryoSPARC^{29,65}. Local refinement reconstructions are shown with a Gaussian filtered map outline to show micelle and AHD densities. The percent contribution of particles from each

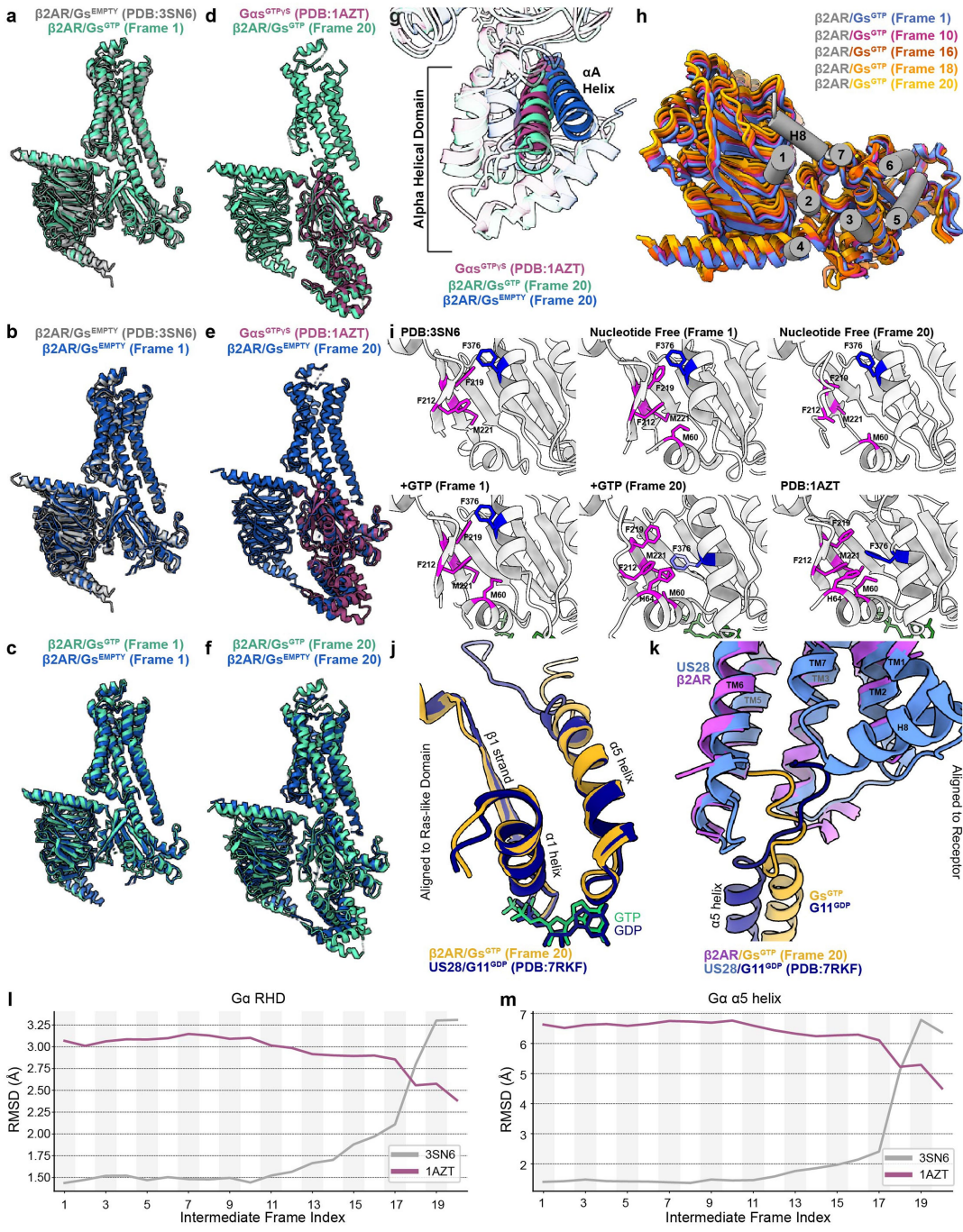
dataset to each local refinement is shown next to each reconstruction (orange, 5 sec.; blue, 10 sec.; green, 17 sec.). **b.**, Local resolution of projections used in final cryo-EM reconstructions. See Supplementary Fig. 1 for associated 3DFSC⁹⁴ curves, directional orientation, power spectra, and angular distribution maps; and see Supplementary Table 2 for a table of sphericity scores.

Article



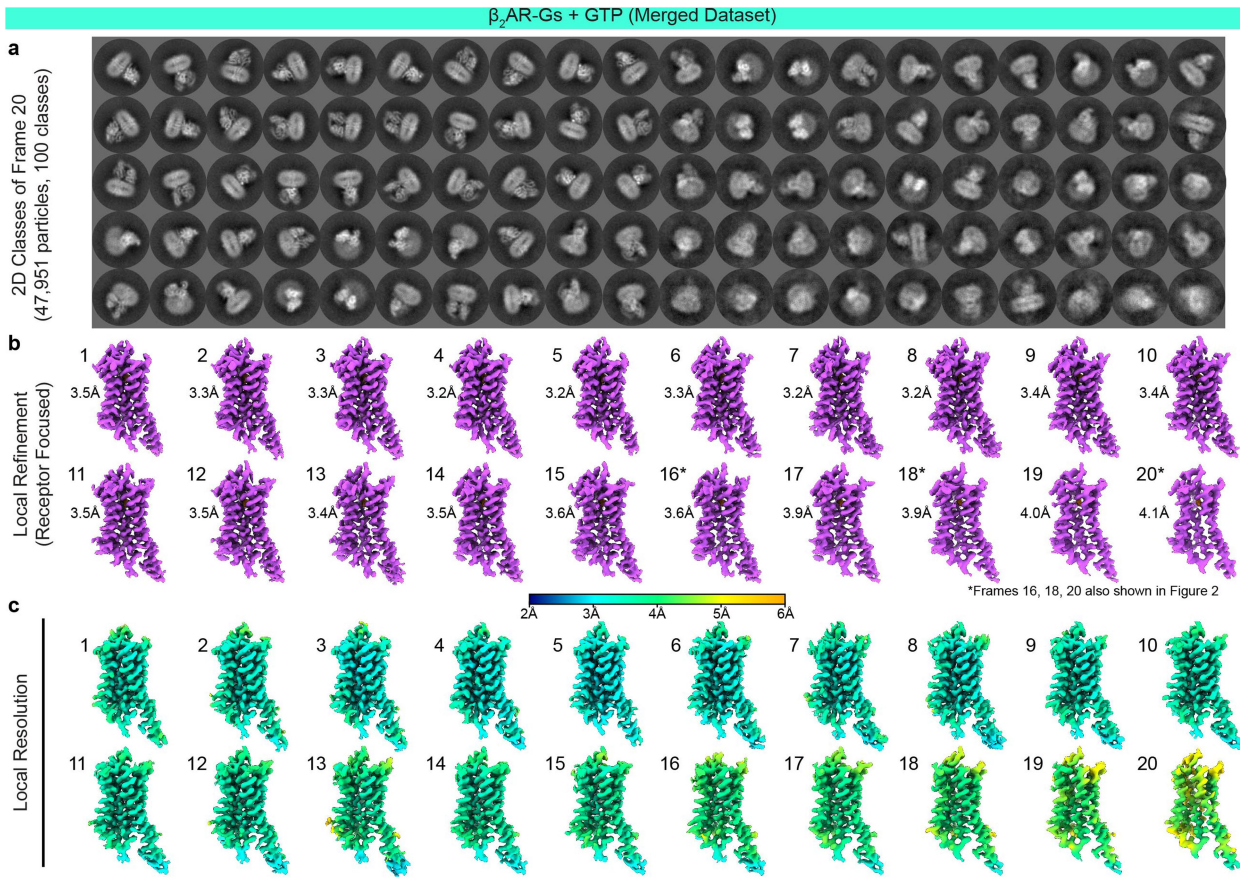
Extended Data Fig. 7 | Cryo-EM processing and reconstruction of $\beta_2\text{AR}-\text{Gs}^{\text{GTP}(\text{Merged})}$ 3D classes. **a**, Continuation of the flow chart in Extended Data Fig. 6 outlining the cryo-EM processing of $\beta_2\text{AR}-\text{Gs}^{\text{GTP}(\text{Merged})}$ complex using cryoSPARC^{29,65}. Local refinement reconstructions are shown with a Gaussian filtered map outline to show micelle and AHD densities. The percent contribution of particles from each dataset to each local refinement is shown

next to each reconstruction (orange, 5 sec.; blue, 10 sec.; green, 17 sec.). **b**, Local resolution of projections used in final cryo-EM reconstructions arising from 3D classification of particles without alignment. See Supplementary Fig. 1 for associated 3DFSC⁹⁴ curves, directional orientation, power spectra, and angular distribution maps; and see Supplementary Table 2 for a table of sphericity scores.



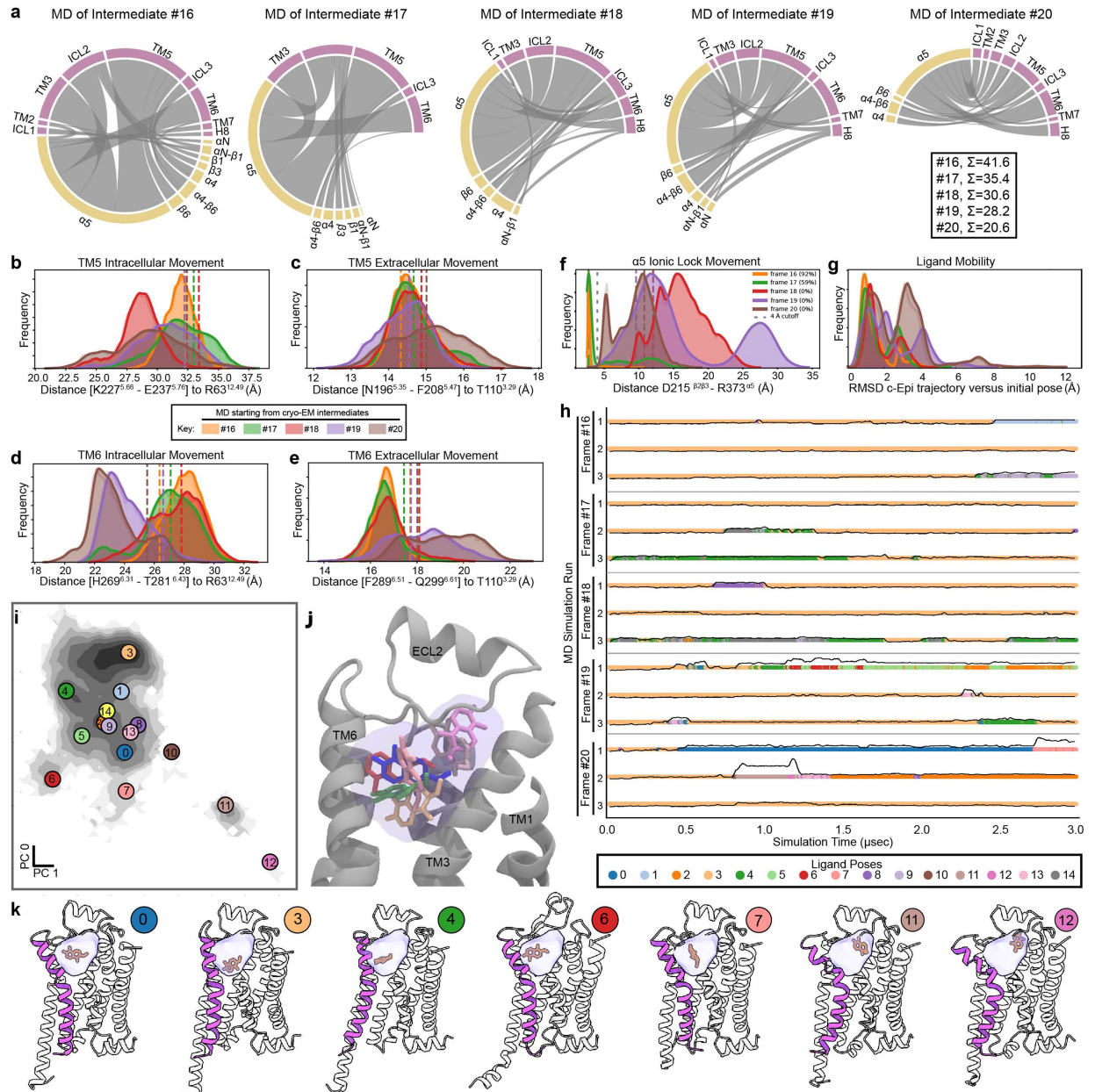
Extended Data Fig. 8 | GTP-bound G_s in the $\beta_2\text{AR}-\text{G}_s$ complex transitions to a similar structure as activated G_s -GTP γ S. **a-g**, Structures comparing the overall architecture of the first and last frames of the $\beta_2\text{AR}-\text{G}_s^{\text{EMPTY}}$ and $\beta_2\text{AR}-\text{G}_s^{\text{GTP}}$ trajectories with ‘checkpoint’ crystal structures of nucleotide free $\beta_2\text{AR}-\text{G}_s$ complex PDB:3SN6 and activated G_s -GTP γ S. Models are aligned to the RHD. **h**, Rotation of G_s in relation to receptor (aligned) over structures of $\beta_2\text{AR}-\text{G}_s^{\text{GTP}}$ cryo-EM structural transition frames. **i**, Placement of $\alpha 5$ Phe in relation to hydrophobic pocket on RHD β -sheets. Rendering style inspired by Jang et al.¹⁹. The residue F376 of Frame 20 (+ GTP condition), in the bottom-middle panel, is translucent blue to indicate it has been built in as a likely position but is stubbed

in our deposited molecular model of that frame. **j-k**, The transition state of US28-G11^{GDP} captured in the process of nucleotide release is similar to that of $\beta_2\text{AR}-\text{G}_s^{\text{GTP}}$ (frame 20). **l-m**, Trace of the root-mean-square-deviation (RMSD) over the 20 $\beta_2\text{AR}-\text{G}_s^{\text{GTP}}$ structural transition frames. Structures have been aligned to the rigid elements of the G_s -RHD, and the RMSD has been computed both for the C α atoms of the whole G_s -RHD (**l**) and just of the $\alpha 5$ helix (**m**). The traces show that for both the G_s -RHD as a whole and the $\alpha 5$ helix, the early frames are structurally closer to PDB:3SN6, whereas the last three frames, from 18 onwards, are closer to PDB:1AZT.



Extended Data Fig. 9 | Local refinement of $\beta_2\text{AR-Gs}^{\text{GTP(Merged)}}$. **a**, 2D class averages arising from the 47,951 particles contributing to frame 20 of the $\beta_2\text{AR-Gs}^{\text{GTP(Merged)}}$ reconstruction sorted into 100 2D classes. All classes appear to have intact receptor micelle and G protein in the complex. **b**, Focused

cryo-EM reconstructions of $\beta_2\text{AR}$ receptor. **c**, Local resolution of projections used in final cryo-EM reconstructions. See Supplementary Fig. 1 for associated angular distribution maps.



Extended Data Fig. 10 | Molecular Dynamics simulations of β_2 AR-Gs^{GTP} intermediate structures. **a** Weakened interactions of β_2 AR and Gs in simulations seeded by later cryo-EM intermediate structures. Chord diagrams show interactions between receptor regions (purple) with Gα regions (gold) coarse-grained to domain segments. Interactions are defined as residue pairs having at least one pair of heavy atoms less than 4 Å apart. Each chord diagram is generated using all the data from triplicate 3 μsec MD trajectories for each seed/condition. The average sum of total contacts for each triplicate #16–20 are 41.6, 35.4, 30.6, 28.2, and 20.6, respectively. **b–g**, Quantification of movement of TM5 (**b**, **c**) and TM6 (**d**, **e**) on the extracellular and intracellular sides of β_2 AR; of the ionic lock with contact frequencies at 4 Å shown inset (**f**), and of c-Epi ligand (**g**). Dashed vertical lines represent values of seed structures. **h**, Sampling

of ligand poses over the MD trajectories shown both as discrete transitions between poses (color-coded time traces, see adjacent ligand pose key below panel), as well as in terms of RMSD to the initial pose (solid black line). **i**, Principal component analysis of the sampled ligand poses, with the positions of selected representative poses superimposed as color-coded circled numbers. **j**, Superimposition of selected ligand poses shown in **i**, showing coverage of the entire ligand binding pocket volume shaded in light purple. **k**, Representative models of selected ligand pose clusters. TM6 shown in solid purple, c-Epi ligand in orange, transparent lilac colored cloud represents the volume sampled by the ligand across all MD trajectories. The extracellular half of TM7 is hidden to show ligand binding pocket. See also Supplementary Table 6 for detailed population information of ligand poses.

Reporting Summary

Nature Portfolio wishes to improve the reproducibility of the work that we publish. This form provides structure for consistency and transparency in reporting. For further information on Nature Portfolio policies, see our [Editorial Policies](#) and the [Editorial Policy Checklist](#).

Statistics

For all statistical analyses, confirm that the following items are present in the figure legend, table legend, main text, or Methods section.

n/a Confirmed

- The exact sample size (n) for each experimental group/condition, given as a discrete number and unit of measurement
- A statement on whether measurements were taken from distinct samples or whether the same sample was measured repeatedly
- The statistical test(s) used AND whether they are one- or two-sided
Only common tests should be described solely by name; describe more complex techniques in the Methods section.
- A description of all covariates tested
- A description of any assumptions or corrections, such as tests of normality and adjustment for multiple comparisons
- A full description of the statistical parameters including central tendency (e.g. means) or other basic estimates (e.g. regression coefficient) AND variation (e.g. standard deviation) or associated estimates of uncertainty (e.g. confidence intervals)
- For null hypothesis testing, the test statistic (e.g. F , t , r) with confidence intervals, effect sizes, degrees of freedom and P value noted
Give P values as exact values whenever suitable.
- For Bayesian analysis, information on the choice of priors and Markov chain Monte Carlo settings
- For hierarchical and complex designs, identification of the appropriate level for tests and full reporting of outcomes
- Estimates of effect sizes (e.g. Cohen's d , Pearson's r), indicating how they were calculated

Our web collection on [statistics for biologists](#) contains articles on many of the points above.

Software and code

Policy information about [availability of computer code](#)

Data collection CryoEM data was collected automatically using SerialEM (ver. 3.6 and 3.9).

Data analysis cryoSPARC (v3.0 and v4.0) was used to process cryoEM data.. UCSF Chimera (ver. 1.16), UCSF ChimeraX (ver. 1.6 & 1.7), and Protein Imager were used to render and visualize structures. 3DFSC was used to calculate FSC curves, directional orientation, power spectra, and sphericity scores. Molecular model was carried out using Coot (version 0.9.8.1 EL) and Phenix (version 1.20.1-4487). GemSpot pipeline utility of Maestro (v.13.8) (Schrödinger) was used to dock ligands. Model analysis was carried out via Python Jupyter Notebooks scripted using the python modules mdclao. CHARMM-GUI builder was used to model and embed the receptor in a lipid bilayer. CgenFF generalized force field was implemented to describe the β 2AR ligand c-Epi. All non-biased simulations were performed using the GROMACS (2022 simulation package). The software VMD1.9, NLG, MDsrv, and mdclao were used to visualize and analyze MD simulations.

For manuscripts utilizing custom algorithms or software that are central to the research but not yet described in published literature, software must be made available to editors and reviewers. We strongly encourage code deposition in a community repository (e.g. GitHub). See the Nature Portfolio [guidelines for submitting code & software](#) for further information.

Data

Policy information about [availability of data](#)

All manuscripts must include a [data availability statement](#). This statement should provide the following information, where applicable:

- Accession codes, unique identifiers, or web links for publicly available datasets
- A description of any restrictions on data availability
- For clinical datasets or third party data, please ensure that the statement adheres to our [policy](#)

The atomic coordinates of β2AR/GsEMPTY (Frames 1-20) have been deposited in the Protein Data Bank under accession codes 8GDZ, 8GE1, 8GE2, 8GE3, 8GE4, 8GE5, 8GE6, 8GE7, 8GE8, 8GE9, 8GEA, 8GEB, 8GEC, 8GED, 8GEE, 8GEF, 8GEG, 8GEH, 8GEI, and 8GEJ, respectively. The atomic coordinates of β2AR/GsGTP(Merged) (Frames 1-20) have been deposited in the Protein Data Bank under accession codes 8GFV, 8GFW, 8GFX, 8GFY, 8GFZ, 8GG0, 8GG1, 8GG2, 8GG3, 8GG4, 8GG5, 8GG6, 8GG7, 8GG8, 8GG9, 8GGA, 8GGB, 8GGC, 8GGE, and 8GGF, respectively; along with the coordinates from corresponding localized maps of β2AR under accession codes 8GG1, 8GGJ, 8GGK, 8GGL, 8GGM, 8GGN, 8GGO, 8GGP, 8GGQ, 8GGR, 8GGS, 8GGT, 8GGU, 8GGV, 8GGW, 8GGX, 8GGY, 8GGZ, 8GHO, and 8GH1, respectively. The atomic coordinates of β2AR/GsGTP(Merged) (Classes A-T) have been deposited in the Protein Data Bank under accession codes 8UNL, 8UNM, 8UNN, 8UNO, 8UNP, 8UNQ, 8UNR, 8UNS, 8UNT, 8UNU, 8UNW, 8UNX, 8UNY, 8UNZ, 8UO0, 8UO1, 8UO2, 8UO3, and 8UO4, respectively.

Cryo-EM maps of β2AR/GsEMPTY (Frames 1-20) have been deposited in the Electron Microscopy Data Bank under accession codes EMD-29951, EMD-29952, EMD-29953, EMD-29954, EMD-29955, EMD-29956, EMD-29958, EMD-29959, EMD-29960, EMD-29961, EMD-29962, EMD-29964, EMD-29965, EMD-29966, EMD-29967, EMD-29968, EMD-29969, EMD-29970, EMD-29971, and EMD-29972, respectively. Cryo-EM maps of β2AR/GsGTP(5sec) (Frames 1-20) have been deposited in the Electron Microscopy Data Bank under accession codes EMD-40096, EMD-40097, EMD-40098, EMD-40099, EMD-40100, EMD-40101, EMD-40102, EMD-40103, EMD-40104, EMD-40105, EMD-40106, EMD-40107, EMD-40108, EMD-40109, EMD-40110, EMD-40111, EMD-40112, EMD-40113, EMD-40114, and EMD-40115, respectively. Cryo-EM maps of β2AR/GsGTP(10sec) (Frames 1-20) have been deposited in the Electron Microscopy Data Bank under accession codes EMD-40116, EMD-40117, EMD-40118, EMD-40119, EMD-40120, EMD-40121, EMD-40122, EMD-40123, EMD-40124, EMD-40125, EMD-40126, EMD-40127, EMD-40128, EMD-40129, EMD-40130, EMD-40131, EMD-40132, EMD-40133, EMD-40134, and EMD-40135, respectively. Cryo-EM maps of β2AR/GsGTP(17sec) (Frames 1-20) have been deposited in the Electron Microscopy Data Bank under accession codes EMD-40136, EMD-40137, EMD-40138, EMD-40139, EMD-40140, EMD-40141, EMD-40142, EMD-40143, EMD-40144, EMD-40145, EMD-40146, EMD-40147, EMD-40148, EMD-40149, EMD-40150, EMD-40151, EMD-40152, EMD-40153, EMD-40154, and EMD-40155, respectively. Cryo-EM maps of β2AR/GsGTP(Merged) (Frames 1-20) have been deposited in the Electron Microscopy Data Bank under accession codes EMD-29985, EMD-29986, EMD-29987, EMD-29988, EMD-29989, EMD-29990, EMD-29991, EMD-29992, EMD-29993, EMD-29994, EMD-29995, EMD-29996, EMD-29997, EMD-29998, EMD-29999, EMD-40000, EMD-40001, EMD-40002, EMD-40004, and EMD-40005, respectively, along with the corresponding localized maps of β2AR under accession codes EMD-40009, EMD-40010, EMD-40011, EMD-40012, EMD-40013, EMD-40014, EMD-40015, EMD-40016, EMD-40017, EMD-40018, EMD-40019, EMD-40020, EMD-40021, EMD-40022, EMD-40023, EMD-40024, EMD-40025, EMD-40026, EMD-40027, and EMD-40028, respectively; and localized G protein maps under accession codes EMD-40156, EMD-40157, EMD-40158, EMD-40159, EMD-40160, EMD-40161, EMD-40163, EMD-40164, EMD-40165, EMD-40166, EMD-40167, EMD-40168, EMD-40169, EMD-40170, EMD-40171, EMD-40172, EMD-40173, EMD-40174, EMD-40175, and EMD-40176, respectively. Cryo-EM maps of β2AR/GsGTP(Merged) (Classes A-T) have been deposited in the Electron Microscopy Data Bank under accession codes EMD-42408, EMD-42409, EMD-42410, EMD-42411, EMD-42412, EMD-42413, EMD-42414, EMD-42415, EMD-42416, EMD-42417, EMD-42418, EMD-42419, EMD-42420, EMD-42421, EMD-42422, EMD-42423, EMD-42424, EMD-42425, EMD-42426, and EMD-42427, respectively.

Raw cryo-EM image data have been deposited in the Electron Microscopy Public Image Archive (EMPIAR) under ascension codes EMPIAR-11855, EMPIAR-11856, EMPIAR-11857, and EMPIAR-11858 for the β2AR/GsEMPTY, β2AR/GsGTP(5sec), β2AR/GsGTP(10sec), and β2AR/GsGTP(17sec) datasets, respectively.

Visualizations of MD trajectories are made available via MDsrv sessions which we have included in a Zenodo dataset associated with this manuscript.

Coordinates of comparison structures were available and obtained through the Protein Data Bank, under accession codes: 3SN6, 1AZT, 7L0Q, and 7RKF.

Research involving human participants, their data, or biological material

Policy information about studies with [human participants or human data](#). See also policy information about [sex, gender \(identity/presentation\), and sexual orientation](#) and [race, ethnicity and racism](#).

Reporting on sex and gender	N/A
Reporting on race, ethnicity, or other socially relevant groupings	N/A
Population characteristics	N/A
Recruitment	N/A
Ethics oversight	N/A

Note that full information on the approval of the study protocol must also be provided in the manuscript.

Field-specific reporting

Please select the one below that is the best fit for your research. If you are not sure, read the appropriate sections before making your selection.

Life sciences Behavioural & social sciences Ecological, evolutionary & environmental sciences

Life sciences study design

All studies must disclose on these points even when the disclosure is negative.

Sample size	Sample sizes were not predetermined by statistical methods. For cryoEM data, sample sizes were determined/limited by time availability of the microscope. These sample sizes were sufficient as they allowed for reconstructing cryoEM maps of the protein complex.
Data exclusions	No data was systematically excluded. Generation of maps from cryo-EM particles involves use of cryoSPARC to sort particles, and remove damaged or poor quality particles to achieve a high-resolution final reconstruction.
Replication	MD simulations were run in triplicate. All replications were successful.
Randomization	No randomization was necessary as simulations were set up using the same parameters.
Blinding	No blinding was necessary. All parameters are set-up by the simulator.

Reporting for specific materials, systems and methods

We require information from authors about some types of materials, experimental systems and methods used in many studies. Here, indicate whether each material, system or method listed is relevant to your study. If you are not sure if a list item applies to your research, read the appropriate section before selecting a response.

Materials & experimental systems		Methods	
n/a	Involved in the study	n/a	Involved in the study
<input checked="" type="checkbox"/>	Antibodies	<input checked="" type="checkbox"/>	ChIP-seq
<input type="checkbox"/>	Eukaryotic cell lines	<input checked="" type="checkbox"/>	Flow cytometry
<input checked="" type="checkbox"/>	Palaeontology and archaeology	<input checked="" type="checkbox"/>	MRI-based neuroimaging
<input checked="" type="checkbox"/>	Animals and other organisms		
<input checked="" type="checkbox"/>	Clinical data		
<input checked="" type="checkbox"/>	Dual use research of concern		
<input checked="" type="checkbox"/>	Plants		

Eukaryotic cell lines

Policy information about [cell lines and Sex and Gender in Research](#)

Cell line source(s)	Spodoptera frugiperda (Sf9) insect cells and Trichoplusia ni (T. ni) insect cells were sourced from Expression Systems.
Authentication	Cells unauthenticated.
Mycoplasma contamination	Mycoplasma contamination not tested.
Commonly misidentified lines (See ICLAC register)	No commonly misidentified lines used.

Plants

Seed stocks	N/A
Novel plant genotypes	N/A
Authentication	N/A